

Differentiation conditions of a basaltic magma from Santorini and its bearing on basaltic-andesite to andesitic magma production in arc settings

J. Andújar, B. Scaillet, M. Pichavant, T.H. Druitt

INTRODUCTION

Caldera forming eruptions are among the most hazardous phenomena occurring on Earth, characterized by the emission of huge amounts of pyroclastic material and gases (e.g. Fish Canyon Tuff, 5000 km³; Bishop Tuff, 600 km³; references?) which can affect the climate at the global scale and be harmful to human life and related infrastructures. This is the case of Santorini volcano, in the Aegean region (Greece), whose explosive activity lead to several caldera forming events, the last and most important of which occurred at around 3.6 ka (the so called Minoan eruption; Druitt et al. 1999), with ~30-70 km³ of ejected rhyodacitic magma. Research studies have been largely focused on the petrogenesis of rhyodacites (i.e., Cottrell et al. 1999; Gertisser et al. 2009). In contrast, comparatively less attention has been paid to the more mafic compositions, although the most recent volcanic activity at Santorini (<200 ka) involved andesite-dominated explosive events (i.e., Upper Scoriae units; Druitt et al. 1999) or effusive activity ranging from dacite to basalt lavas. Therefore, the conditions of evolution from basalt to the most silica-rich compositions are still unclear. A recent petrological study suggests that basalt to rhyodacite melt evolution occurs in different reservoirs located at different depths below the volcano (Druitt et al. 2012); whereas other studies have concluded that rhyodacitic compositions are generated in a unique reservoir at a constant depth (e.g., Gertisser et al. 2009). Thus, to improve our knowledge on andesitic volcanism at Santorini in particular, but also in arc settings in general, we have experimentally investigated the phase relationships of a representative basalt from Santorini with the aim of determining the conditions of differentiation (pressure, temperature, volatile fugacities) and its putative parental relationships with andesitic magmas erupted there. Our results show that basalts coming from the mantle stagnate at depths of 12-14 km (400 MPa), where they fractionate to yield basaltic andesite liquids at 1000°C (55 to 58 wt% SiO₂) and $fO_2 \sim FMQ-0.5(\pm 0.3 \text{ log units})$ containing ~3 wt% H₂O_{melt} by crystallizing $\geq 60\text{wt\%}$ of olivine (ol), clinopyroxene (cpx), plagioclase (plag), orthopyroxene (opx), Ti-rich magnetite \pm pigeonite (pig), ilmenite (ilm). The comparison with andesites from Santorini suggests that such conditions do not correspond to the final storage conditions for andesite and that an increase in oxygen fugacity or a migration+oxidation probably occurred prior to the andesitic eruptions.

GEOLOGICAL SETTING

The geology and tectonics of Santorini have been the focus of many studies which are briefly summarised below. Santorini island belongs to the Cyclades archipelago, and is the most active volcanic complex of the South Aegean volcanic arc, which is related to the north-east subduction between the Aegean sea and African plate (Druitt et al. 1989). The island rests on a 32 km thick continental crust made of Mesozoic to Cenozoic marbles and phyllites (Nichols, 1971b). The volcanic history of Santorini comprises more than 100 eruptive events over the

past 400 ka, including several caldera collapses episodes, such as the so called Minoan eruption, some 3.6 ky ago. Four main eruptive cycles have been identified (Druitt et al., 1999), the three oldest of which present calc-alkaline affinities and outcrop at the Akrotiri peninsula and northern Thera. The products of the youngest eruptive cycle (Thera pyroclastic formation) have a tholeiitic character which contrasts with that of the oldest cycles (Druitt et al. 1999). After the last caldera event, volcanic activity resumed at 197 BC being centred in the intra-caldera area, and continuing until recent times (Parks et al. 2012). The products of this historical volcanism at Santorini built the Palea Kameni and Nea Kameni islands.

The volcanic products at Santorini range from basalts to rhyodacites, with some rare rhyolites (Nichols, 1971a; Druitt et al. 1999). Based on the dominant type of magma ejected the Santorini explosive events from the youngest Thera pyroclastic formation can be categorized into two main types: andesite dominated and silicic-dominated eruptive cycle, each one associated to differences in volcanic activity and chemical arrays of the erupted products (Druitt et al. 1999). According to Druitt et al (1999), the intermediate dominated eruptions reflect a reservoir where the dominant volume magma was andesitic in composition, overlain by one or more layers of dacite or evolved andesite (i.e., Upper Scoriae 1 and 2 units). In contrast, in silicic eruptions the reservoirs were dominated by a rhyodacitic magma which was intruded by basalt or mafic-andesite just prior to eruption, this last found as mafic blebs dispersed within the main silicic volume (Nichols, 1971a; Huijsmans et al. 1988; Druitt et al. 1999; Cottrell et al. 1999; Gertisser et al., 2009).

Previous constraints on storage conditions

Constraints on pre-eruptive conditions from Santorini products were mainly obtained by applying geothermometers and mineral-liquid equilibria, except for the Minoan eruption for which experimental phase equilibria were established by Cottrell et al. (1999). Co-existing Fe-Ti oxides in dacitic to rhyodacitic products yield temperatures between 825-985°C (Gardner et al. 1996, Druitt et al. 1999; Cottrell et al. 1999; Gertisser et al. 2009; Cadoux et al., 2013a,b). Estimates for the more mafic compositions (50-60 wt% SiO₂) based on olivine-melt and clinopyroxene-orthopyroxene geothermometers yield temperatures between 980-1030°C for andesites (i.e.; 1000°C for Upper Scoriae 1; Gardner et al. 1996) and up to 1200°C for basaltic compositions (Gertisser et al. 2009; Huijsmans 1985). Such estimates are in general agreement with those obtained by Michaud et al. (2000), based on melt inclusions homogeneisation during heating stage experiments, which yield temperatures of 850-900°C for rhyodacites, 985-1005°C for andesites, and 1085-1105°C for basalts. Magmatic water contents (H₂O_{melt}) were estimated by FTIR analysis on melt inclusions and by experimental phase equilibria on the Minoan rhyodacitic products. Melt inclusions from the Upper Scoriae 1 and mafic blebs in the Lower Pumice 2 eruption yield H₂O_{melt} of about 3 and 3.8 wt%, respectively (Gardner et al 1996; Gertisser et al. 2009), whereas H₂O_{melt} of rhyodacitic magmas range from 3-4.5 wt% (Minoan, Lower Pumice 2) up to 6 wt% (Cottrell et al. 1999; Gertisser et al. 2009; Cadoux et al., 2013a,b). Pressures estimates using Al-in hornblende and phase equilibrium experiments on rhyodacitic eruptions yield values between >200 and 400 MPa (Gertisser et al. 2009; Cottrell et al. 1999; Cadoux et al., 2013a,b) though according to Cottrell et al. (1999) the Minoan magma raised at shallower levels (50 MPa) a few months

prior to the eruption. Lastly, fO_2 estimates by co-existing Fe-Ti oxides range between FMQ-0.5 (0.5 log unit below the Fayalite-Magnetite-Quartz buffer) and NNO+0.5 (0.5 log unit above the Ni-NiO buffer) for mafic to silicic compositions (Gertisser et al. 2009; Cottrell et al. 1999; Cadoux et al., 2013a,b).

Petrologic observations of selected samples

To constrain the conditions of storage and evolution of basaltic magmas at Santorini, we have performed phase equilibrium experiments on a basaltic sample from the Balos Bay cinder cone (344 ka; Fig.1; Druitt et al. 1999), of the Akrotiri-Thira main volcanic series (Nicholls, 1971a). The experimental products were compared with the major explosive Upper Scoriae 1 andesitic eruption (Fig.1; Druitt et al. 1999). Bulk rock compositions of both rocks (Balos Bay basalt and Upper Scoria andesite), were obtained by inductively coupled plasma mass spectrometry analysis (ICP-MS), agreeing with previous studies (Nicholls, 1971a; Druitt et al. 1999). Several thin sections were prepared for observation with the petrographic and scanning electron microscopes (SEM). The composition of the main mineral phases was then determined by electron microprobe analyses (EMPA), and the results are shown in Tables 1 and 2 and Figures 2 to 7.

Basaltic sample

The combination between mineral densities and scanning electron microscope (SEM) image analysis of the thin sections from the natural sample shows that the Balos basalt (Table 1) contains 40 wt% of phenocrysts with 7 wt% of euhedral to partially resorbed phenocrysts of olivine (0.5-1 mm, Fo₇₅), set in a crystallized matrix of 32 wt% of plagioclase (An₇₉), 2 wt% of clinopyroxene (En_{43±2.6}Fs_{11±1.2}Wo_{45±3.5}, Mg#80±1.6), traces of magnetite (Mg# 0.6), occasional ilmenite (Mg#1.4; 50.5 TiO₂ wt%) and orthopyroxene/pigeonite (En₆₉Fs₂₂Wo_{7.8}, Mg#: 76; Fig.2). In detail, olivine phenocrysts show little compositional variation (Fo₇₄₋₇₆) between and within crystals (Fig. 2b). However, some rare resorbed phenocrysts showing slight inverse zoning from Fo₇₆ to Fo₇₇ are also present (Fig 2b). Apart from clinopyroxenes in the matrix, a few resorbed and reversely zoned phenocrysts (~500 µm) occur, with core En₄₂Fs₁₀Wo₄₇ (Mg#80) and rim En₄₄Fs₈Wo₄₈ (Mg#84) (Appendix-1). Two different populations of plagioclase can be distinguished: one population with sizes of ~500 µm has An₈₅₋₉₀ cores and narrow An₇₉ rims, whereas plagioclase in the matrix (~300-50 µm) has An₇₈₋₈₀ cores and An₇₂ rims (Fig. 2d).

Andesitic sample: Upper Scoriae 1

The Upper Scoriae 1 andesite (Table 2) has pyroxenes, plagioclase, magnetite phenocrysts, and lesser amounts of olivine, which are set in a highly vesiculated and microcrystalline groundmass of plagioclase, clinopyroxene and magnetite (Fig. 3a).

Pyroxenes

Pyroxenes display a wide range of compositions as well as complex textural features. In detail, augite, diopside, pigeonite and orthopyroxene crystals were identified within the natural andesite (Table 2; Fig. 4a). The modal distribution of the Mg# shows four distinct

populations (Figs. 4b), the most important population having Mg# between 61 and 71, whereas three minor peaks are found at Mg#58, Mg#75 and Mg#81.

Augite is found as euhedral to subhedral crystals having sizes between 50-150 μm ; the dominant population have an average composition of $\text{En}_{42}\text{Fs}_{21}\text{Wo}_{37}$ Mg# 67 ± 1 (Table 2, Figs. 3 and 4b,c) and appears as isolated, or normally zoned crystals (cores of $\text{En}_{44}\text{Fs}_{19}\text{Wo}_{37}$ Mg#70 to rims of $\text{En}_{42}\text{Fs}_{21}\text{Wo}_{37}$ Mg# 67 ± 1) or also, as a part of reversal compositional zoning (cores of $\text{En}_{38}\text{Fs}_{23}\text{Wo}_{39}$ Mg#63 to rims $\text{En}_{42}\text{Fs}_{21}\text{Wo}_{37}$ Mg# 67 ± 1 , Figs. 4, 6c Appendix-2).

Orthopyroxene crystals have sizes of $\sim 200\ \mu\text{m}$ and are characterised by presenting resorbed borders or cores with composition $\text{En}_{55}\text{Fs}_{40}\text{Wo}_4$, Mg#58, mantled by $\text{En}_{65}\text{Fs}_{29}\text{Wo}_4$, Mg#68 composition (Fig.6); this last also appears in contact with augites of composition $\text{En}_{44}\text{Fs}_{19}\text{Wo}_{37}$ Mg#70 and $\text{En}_{42}\text{Fs}_{21}\text{Wo}_{37}$ Mg# 67 ± 1 (Fig. 6c). Such a textural relationships and the lack of reaction-rims between the Mg-rich orthopyroxene and the augites with Mg#67-70, suggest a process of co-crystallization between these phases.

Pigeonite has compositions varying from $\text{En}_{55}\text{Fs}_{28}\text{Wo}_{16}$ Mg#67 to $\text{En}_{60}\text{Fs}_{30}\text{Wo}_8$ Mg#67 (Table 2; Fig. 5) and appears as isolated partially resorbed crystals or as cores in pyroxene which are mantled by a normally zoned augite from $\text{En}_{44}\text{Fs}_{19}\text{Wo}_{37}$ Mg#70 to $\text{En}_{42}\text{Fs}_{21}\text{Wo}_{37}$ Mg#67 (Figs.5a-e).

Diopsides with composition $\text{En}_{43-45}\text{Fs}_{10-14}\text{Wo}_{43-45}$, Mg#75-81 are present as 500 microns to up to 1 mm euhedral to partially rounded crystals showing small compositional variations all over their length but some of them present narrow rims that reach the main augite composition (Figs. 4d, Appendix 2).

Plagioclase, magnetite and olivine

Plagioclase occurs as two distinct populations (Fig. 7a): 1) euhedral crystals (100 to 300 μm) with near uniform composition ($\text{An}_{53\pm2.5}$; Table 2; Fig.7) and 2) zoned crystals ($\geq 500\ \mu\text{m}$) with cores of $\text{An}_{91\pm2.7}$ and narrow rims of An_{53} , An_{60} and An_{75} (Figs. 3d and 7b).

Magnetite is homogeneous in composition with Mg#2 and TiO_2 contents of 15 wt% (Table 2) whereas, olivine appears as partially resorbed crystals with sizes between 50 and 150 microns, having compositions of Fo_{63} and Fo_{68} (Table2, Figs 3b and e)

Residual liquid

The petrographic study and the compositions of the different minerals present in the USC-1 andesitic sample allow us to identify the mineral assemblage of this rock so as to calculate its crystal content (wt%) by combining SEM-image analyses of thin sections and mineral densities (Deer et al. 1972). It appears that the USC-1 sample contains 28 wt% of phenocrysts with euhedral to subhedral plagioclase (16 wt%, An_{53}), augite (8 wt%, $\text{En}_{42}\text{Fs}_{21}\text{Wo}_{37}$, Mg#67), magnetite (3 wt%) and lesser amounts of orthopyroxene (1.4 wt%, $\text{En}_{65}\text{Fs}_{29}\text{Wo}_4$). These phase proportions and compositions were then used to calculate by mass balance the coexisting residual melt composition. The resulting melt is andesitic in composition with 63 wt% SiO_2 , 7 wt% FeO^* , 1.8 wt% MgO and 6.6 wt% ($\text{Na}_2\text{O}+\text{K}_2\text{O}$) (Table 2). The calculated liquid

composition falls between those analysed by Druitt et al. (1999) for USC-1 products which range between andesitic (60 wt% SiO₂) to dacitic (65 wt%) composition.

Origin of crystals

A xenocrystic origin of olivine, pigeonite, diopside En₄₃₋₄₅Fs₁₀₋₁₄ Wo₄₃₋₄₅, Mg#75-81 and An-rich plagioclase (An₉₁) crystals found within the USC-1 sample, is supported by the following lines of evidence; (1) both pigeonite and olivine readily crystallise from the basalt (see below, experimental results), (2) the composition and chemical profiles of diopside and Ca-rich plagioclase found in the andesite are identical to those diopside and plagioclase of Balos basalt (Figs. 2c, 4a and 7) indicating that these mineral compositions likely derive from a more mafic magma; (3) the frequent presence of narrow rims matching the composition of the main augite-plagioclase population suggests reequilibration with the host andesitic melt, yet, the lack of such rims or resorbed textures on some olivine and pigeonite (Figs. 3 to 7) shows that not all xenocrysts had time to react; (4) the resorbed texture of En₅₅ Fs₄₀ Wo₄, Mg#58 orthopyroxenes in andesite and the fact that they are commonly mantled by a more Mg-rich composition suggest also a xenocrystic origin, such orthopyroxenes being similar to those of Santorini dacites. However, change in storage conditions may also explain these low-Mg orthopyroxene crystals.

We conclude that, to a first approximation, the An₅₃ plagioclase, En₄₂Fs₂₁Wo₃₇, Mg# 67 augite, magnetite and En₆₅Fs₂₉Wo₄, Mg#68 orthopyroxene crystallized from the andesitic magma, whereas high-Ca plagioclase, pigeonites, diopsides, En₅₅Fs₄₀Wo₄, Mg#58 orthopyroxene and olivines are xenocrystics. Thus, we have calculated the amount of xenocrysts present within the sample to estimate the effect of these phases on the whole-rock composition, following the same procedure that was used to calculate the proportion of phenocrysts present in the andesite (see above). The results indicate that, despite of the large sizes that characterize these crystals (>1 mm, i.e., diopsides of Fig. 3), they do not represent more than the < 1.5 vol% of the whole sample and so have little compositional leverage on the bulk-rock andesitic composition. This indicates that the bulk-rock composition of the andesitic scoria can be taken as representative of a liquid composition; this is an important assumption for crystallization experiments to determine magma pre-eruptive and melt evolution conditions at Santorini volcano (see Pichavant et al., 2007).

EXPERIMENTAL APPROACH AND ANALYTICAL TECHNIQUES

The starting dry glass for our experimental study was obtained by crushing and milling several pieces of basaltic sample (about 10 gr) followed by a two step fusion of the resulting powder (with grinding in between) in a Pt crucible at 1400°C at atmospheric pressure for three hours. Electron microprobe of the dry glass showed it to be homogeneous and similar to the XRF determination (Table 1). The basaltic glass was then ground and stored at 120°C in an oven to avoid atmospheric hydration.

Capsule preparation

The starting powder was loaded into 1.5 cm long, 2.5mm inner diameter, 0.2 wall thickness Au capsules to minimize Fe loss under reduced conditions. All capsules were prepared following the procedure described by Scaillet et al. (1995) and Andújar and Scaillet (2012) where H₂O is added first, followed by silver oxalate as source for CO₂ in H₂O-undersaturated runs. The amount of H₂O+CO₂ added to the capsule and the fluid/silicate ratio were maintained constant by adding 3±0.5mg of fluid (H₂O+CO₂) and 30 mg of glass powder, which ensures that fluid-saturated conditions were always achieved (Andújar and Scaillet, 2012, Scaillet et al., 1995).

The capsules were then arc-welded and left in an oven at 100°C for few hours to homogenise H₂O distribution within the charge before the experiments. For all charges reported in Table 3, the weight of the capsules prior to and after the experiments agreed to within 0.0004 g of each other. This weight difference is about the precision of the analytical balance, and confirms that no fluid escaped during the experiments.

For each run, different XH₂O_{in} [=initial H₂O/(H₂O+CO₂)in moles] were explored by means of adding different starting H₂O-CO₂ mixtures to the capsule so as to cover an XH₂O_{in} range of 1-0.12 (water-saturated to “nominally” dry conditions, Table 3).

Experimental equipment

All experiments were conducted in a vertical Internally Heated Pressure Vessel (IHPV) pressurized with different mixtures of Ar+H₂ at room temperature to achieve the desired *f*O₂ conditions. A double-winding molybdenum furnace was used to achieve near-isothermal conditions (gradient <2-3°C) along a 3 cm long hotspot. Temperature was measured using three S-type thermocouples with an accuracy of ±5°C, whereas total pressure was recorded by a transducer characterized by an uncertainty of ±20 bars. Typically, each experiment was loaded with a set of five basalt+H₂O+CO₂ charges plus one capsule containing a Ni-Pd-O or Co-Pd-O (depending on the desired *f*O₂, Taylor et al. 1992) redox sensor, which was used to monitor the prevailing *f*H₂ at the desired T-P (Table 3). The set of capsules were run at the selected T-P-*f*H₂ for about 24 hours and terminated by using a drop quench device (Di Carlo et al., 2006). In all runs reported in Table 3 a rise in the total pressure was observed at the end of the experiment, showing that the sample holder had fallen into the bottom cold part of the vessel and that the drop quench was successful (quench rate >100°C/s). After the experiments capsules were checked for leaks, opened and some pieces of the run products were embedded in epoxy resin and polished for optical observation, and subsequent SEM and EMP analyses.

Water content, *f*H₂, *f*O₂ in the experimental charges

The procedure followed in this work for capsule preparation ensures fluid-saturated conditions for each charge. However, the relatively low amount of fluid phase used to minimise silicate dissolution into the fluid resulted in the impossibility of obtaining direct measures of the final H₂O-CO₂ composition in the fluid phase. In addition, the majority of the charges were characterised by a high crystal content (>30 wt%; Table 3) and homogeneous distribution of the mineral phases (see below) which prevented direct H₂O determination by IR-measurements. Hence, the H₂O_{melt} of each experimental run was calculated by using the

water-solubility model of Papale et al. (2006) and the $\text{XH}_2\text{O}_{\text{in}}$ of each run, which is equivalent to assuming ideal behaviour in the H_2O - CO_2 fluid phase (e.g., Berndt et al., 2005; Andújar and Scaillet, 2012). Whenever possible, we have compared the Papale's model results with those obtained with the "by difference method" which were obtained from the summatory difference of the corresponding EMP analyses of residual liquids after alkali-migration correction (Table 3; see below). The results show that these two different approaches agree within analytical errors. Once the water content is known, the H_2O activity ($a_{\text{H}_2\text{O}}$) of each charge was calculated by using the solubility model of Burnham (1979), and then the corresponding water fugacity ($f_{\text{H}_2\text{O}} = a_{\text{H}_2\text{O}} f^{\circ}_{\text{H}_2\text{O}}$; $f^{\circ}_{\text{H}_2\text{O}}$ being the fugacity of pure water at the relevant P-T, see Scaillet et al., 1995; Freise et al., 2009; Andújar and Scaillet, 2012). Subsequently, the prevailing f_{O_2} of each charge was determined by knowing the intrinsic f_{H_2} (obtained from the Ni-Pd-O, Co-Pd-O sensors), the dissociation constant of water (from Robie et al. 1979) and the $f_{\text{H}_2\text{O}}$ at the experimental pressure and temperature (i.e., Di Carlo et al., 2006; Andújar and Scaillet, 2012). Results are shown in Table 3. It is worth noting that, at each P-T- f_{H_2} , the f_{O_2} varies with temperature and decreasing $a_{\text{H}_2\text{O}}$ (or $\text{XH}_2\text{O}_{\text{in}}$) (for more details see Scaillet et al., 1995; Freise et al., 2009; Andújar and Scaillet, 2012).

Experiments were performed in the range of temperatures 975-1040°C but at two different oxidation states: 1) under oxydizing conditions with oxygen fugacities ranging from NNO+0.5 to NNO-1.65 (hereafter referred to as NNO experiments) and 2) under slightly reducing conditions, in which f_{O_2} varied between FMQ+0.6 to FMQ-3 (hereafter referred to as FMQ experiments). In addition, an extra set of experiments was conducted at highly oxydizing conditions with an $f_{\text{O}_2} \sim \text{NNO} + 3.5$ (Table 3).

Analytical techniques

Microprobe analyses were obtained with a cameca SX-50 electron microprobe apparatus at ISTO-BRGM in Orléans and with a JEOL JXA-8200 super probe at the University of Huelva using an acceleration voltage of 15 kV, sample current of 6 nA, and 10s as counting time. A focused beam was employed for analysing the mineral phases, whereas a defocused 10 microns beam was used with glasses to minimize alkali migration (i.e., Morgan and London, 2005; Di Carlo et al. 2006). In addition, the crystal-free charge s069-1 was analysed first in each probe session to quantify and correct the alkali effect with the "by difference" method for the determination of $\text{H}_2\text{O}_{\text{melt}}$ in crystal-bearing runs.

Attainment of equilibrium

In this study we have only performed crystallization experiments. As in previous similar studies (e.g., Di Carlo et al., 2009; Freise et al., 2009; Pichavant et al., 2009), several observations demonstrate that near-equilibrium conditions were attained during the experiments: the euhedral shape of crystals, the homogeneous distribution of phases within the charges, the smooth variation of phase proportions and compositions with changes in experimental conditions, and the small sum of residuals (generally < 0.5 ; Table 3) from mass balance calculations, the latter indicating that no major phase has been omitted. Moreover, run durations (≤ 24 hours) are within the range of other studies performed on basaltic

compositions for which near-equilibrium conditions have been also claimed (e.g., Di Carlo et al., 2006; Freise et al., 2009).

RESULTS

Identified mineral phases in the run products include olivine, clinopyroxene, magnetite, plagioclase, pigeonite, ilmenite and amphibole. Phase proportions were obtained by mass-balance calculations using the bulk-rock composition and the composition of the different phases present in the charge. The results are listed in Table 3 and displayed in a series of polybaric-isothermal or isobaric polythermal panels which show the effects that the variation of T, P, H₂O content and fO_2 have on phase relationships (Fig. 8).

Phase relations at fO_2 ~NNO

At 200 MPa, under oxydizing conditions (Fig. 8a) the phase assemblage is dominated by olivine, clinopyroxene, plagioclase and magnetite, liquidus conditions being reached at 1040°C for H₂O_{melt} > 6 wt%. Below 1000°C amphibole crystallizes, being in a reaction relationships with both olivine and clinopyroxene in the water-rich part of the diagram (H₂O_{melt} >3 wt%). At lower H₂O_{melt} amphibole is replaced by orthopyroxene, which is stable only below 1000°C, being in a reaction relationships with olivine in the dry region (Fig. 8). At 200 MPa, an increase in fO_2 from ~NNO (Fig. 8) to NNO+3.5 shifts orthopyroxene stability to higher temperatures (1040°C; Table 3).

Phase relations at fO_2 ~FMQ

The same assemblage occurs at near liquidus conditions at 200 MPa and FMQ, except that the magnetite in-curve is slightly lowered compared to NNO. Amphibole is stable at H₂O_{melt} > 5 wt%, where it crystallizes with olivine and clinopyroxene. Ilmenite is also present at temperatures below 980°C, whereas it is absent at NNO. Increasing pressure to 400 MPa produces a marked depression of plagioclase stability curve, so that this phase crystallises at H₂O saturation below 980°C. Similarly the stability field of magnetite is significantly displaced down temperature, appearing after ilmenite whose stability field is also displaced toward lower H₂O_{melt}. Orthopyroxene (+pigeonite) crystallises at H₂O_{melt} < 5 wt%, as observed at 200 MPa and NNO, but at these more reduced conditions, persists up to 1040°C. The stability field of amphibole is broadly similar in shape to that at 200 MPa, this phase being in a peritectic relationships with olivine and clinopyroxene down temperature.

The polybaric-isothermal section at 1000°C, shows that orthopyroxene (+pigeonite), and possibly ilmenite, both react out between 400 and 200 MPa, if the magma decompression occurs at this temperature for H₂O_{melt} in the range 3-5 wt%, whilst magnetite may crystallise during magma uprise.

Phase proportions

The crystal content of the experimental charges varies systematically with H_2O_{melt} , increasing with decreasing H_2O_{melt} . Liquidus conditions were attained at 1000°C, 200 MPa and 6 wt% H_2O_{melt} , whereas the highest crystal content (83 wt%), as determined by mass-balance calculations, was reached at 1040°C/200 MPa/NNO and 1 wt% H_2O_{melt} (Fig.9; Table 3). At constant temperature, H_2O_{melt} and oxygen fugacity (i.e., 1000°C, FMQ series), the general trend is to increase the crystal content with increasing pressure, an effect which is enhanced in the pressure range 200-400 MPa (Fig. 9). Magnetite, orthopyroxene and pigeonite are present in lower concentrations (<3 wt%) compared to olivine and clinopyroxene abundances. However, the proportions of these two phases increase moderately with decreasing H_2O_{melt} or temperature when compared to that of plagioclase, which rapidly becomes the dominant phase (Table 3).

Phase compositions

Experimental phase compositions are reported in Tables 4 to Table 8, whose variations with P-T- fO_2 and H_2O_{melt} are discussed below.

Olivine

Olivine composition systematically varies with temperature, water content, oxygen fugacity, degree of crystallization and composition of the coexisting melt (Table 4; Fig. 10). In the range of explored T, P, fO_2 and H_2O_{melt} , olivine composition varies between Fo90 and Fo64, the highest content being reached at high fO_2 (NNO+3.5) and high temperature (e.g., charge 1040°C, 200 MPa, NNO+3.5) whereas the lowest occurs at 1000°C, 400 MPa, FMQ and 1.8 wt% H_2O_{melt} . At a given pressure, the Fo content decreases with decreasing H_2O_{melt} and temperature. An increase in fO_2 increases the Fo content, however, the effect of fO_2 is enhanced at 400MPa and high H_2O_{melt} (9 wt%), where the Fo content decreases by about 15 mole% from NNO to FMQ. In general, at a given temperature and H_2O_{melt} , an increase in pressure decreases the Fo content (i.e., differences >10 mole %) though the effect on olivine composition remains modest when pressure changes from 100 to 200 MPa at 1040°C, compared to the effect seen in the pressure range 200-400 MPa at 1000°C and 975°C.

As shown in previous studies, olivine composition varies with melt composition and hence, with the degree of crystallization (e.g., Berndt et al., 2005; Di Carlo et al., 2006). The Fo content decreases with the CaO/Al₂O₃ ratio or Mg# of coexisting melt (e.g., Di carlo et al. 2006; Pichavant et al. 2002) (Fig.10). The CaO content in olivine is generally accepted as a faithful indicator of degree of evolution of olivine (Libourel, 1999) and at a given temperature it increases with decreasing H_2O_{melt} , X_{Fo} and CaO/Al₂O₃melt (Table 4; Figs. c-e), in agreement with other experimental studies (Berndt et al. 2005; Di Carlo et al. 2006). The average olivine-liquid exchange coefficient $K_d^{\text{Fe-Mg}}$ olivine/liquid is 0.27 ± 0.04 when calculated with $\text{FeO} = \text{FeO}_{\text{total}}$ and 0.30 ± 0.04 when calculated with $\text{Fe}^{2+}/\text{Fe}^{3+}$ of the coexisting liquid estimated with the method of Kress and Carmichael (1991). These values are close to those found in similar studies (0.28–0.33, Sisson & Grove, 1993a; 0.33, Pichavant et al., 2002; 0.28, Barclay & Carmichael, 2004).

Our results show that Olivine composition is sensitive to changes in T , H_2O_{melt} and fO_2 thus; it is possible to use the composition of experimental olivines to calibrate the dependence of crystallizing olivine composition as function of these parameters by using minimum square difference methodology; we have obtained the following expression:

$$\text{Eq. 1: } Fo (\text{mol}\%) = 0.1302 * T + 1.9121 * H_2O_{\text{melt}} + 2.8677 * \Delta NNO - 66.01$$

Clinopyroxene

Experimental clinopyroxenes are augites and diopsides with composition $En_{40-49}Fs_{7-23}Wo_{27-46}$, and $Mg\#$ 68-87. (Table 5). The clinopyroxenes with higher $Mg\#$ are found at 1040°C, 400 MPa, FMQ and 9 wt% H_2O_{melt} and 1040°C, 200MPa, $NNO+3.5$ and 3 $H_2O_{\text{wt}\%}$ melt. It is noteworthy that clinopyroxene composition is strongly correlated with H_2O_{melt} (hence crystal content or melt composition): at a given temperature, a decrease of H_2O_{melt} from 7 to 2 wt% increases by about 10 mol% the En and Fs contents and decreases the Wo content by the same magnitude. Changes in temperature, pressure or oxygen fugacity (from NNO to FMQ) have comparatively smaller effects (< 5 mol%). The Kd^{Fe-Mg} of clinopyroxene/liquid pairs range between 0.19 and 0.41 with a mean value 0.28, again in agreement with previous experimental works conducted on similar compositions (Berndt et al. 2005; Di Carlo et al. 2006, Pichavant et al. 2002). The Kd^{Fe-Mg} varies linearly with the $Mg\#$ of the melt ($Kd_{\text{cpx}} = (0.0076 * Mg\#_{\text{melt}}) - 0.073$, $R^2 = 0.78$; Appendix 3), variations in fO_2 , T or P having little effect on this parameter (e.g., Toplis and Carroll, 1995). We have found that for clinopyroxenes the Wo content has little dispersion with the variation in the experimental variables and hence, it can be expressed as:

$$\text{Eq.2: } Wo(\text{mol}\%) = 0.0079 * T + 1.1261 * H_2O_{\text{melt}} + 0.2721 * \Delta NNO + 28.30284$$

Orthopyroxene and pigeonite

At 200 MPa and NNO, orthopyroxene composition is in the range $En_{87-83}Fs_{10-13}Wo_{3-4}$, and $Mg\#$ 90-87 whereas at FMQ it is $En_{64-76}Fs_{20-29}Wo_{3-6}$, and $Mg\#$ 69-79 (Table 6; Fig. 12). At 400 MPa and FMQ pigeonite has composition $En_{59-52}Fs_{21-26}Wo_{15-24}$ and $Mg\#$ 67-73. Temperature decreases En and Wo contents as well as $Mg\#$, and increases the Fs content of both orthopyroxene and pigeonite. A decrease in H_2O_{melt} decreases En and $Mg\#$, and increases Wo content though for pigeonite the variation of its Wo content with H_2O_{melt} is less apparent (Fig. 12). Our data set on the effect of fO_2 on orthopyroxene composition is quite limited but it appears that a decrease in fO_2 from $NNO+3.5$ to FMQ-2 (at constant H_2O_{melt}) decreases the En and $Mg\#$ and increases the Fs content of orthopyroxene whereas Wo is not affected (Fig. 12).

Plagioclase

The composition of experimental plagioclases (Table 7) as a function of H_2O_{melt} is shown in Fig 13. Plagioclase composition ranges from An89 to An58, the highest value being reached at 200 MPa, 1000°C, and 6 wt% H_2O_{melt} , while the lowest one is produced at 400 MPa, 1000°C, 2 wt% H_2O_{melt} , both at FMQ. At a given T, P and fO_2 conditions, both the Ab and Or contents increase with decreasing water content in the melt (hence increasing crystal content), in agreement with previous studies (e.g., Berndt et al., 2005; Sisson and Grove 1993a,b). At fixed temperature, H_2O_{melt} and fO_2 , variations in pressure do not affect significantly plagioclase composition, except at 975°C and FMQ, at which a pressure increase from 200 to 400 MPa decreases An by 15 mol%. In general, plagioclase crystallising at high fO_2 tends to be slightly less calcic (compare NNO and FMQ runs at 200 MPa and 1000°C, Fig. 13). The plagioclase-liquid Ca-Na exchange varies between 0.99 and 5.1 with a mean value of 2.23, in good agreement with previous studies on hydrous basaltic compositions (Pichavant et al., 1999; Di Carlo et al. 2006; Berndt et al. 2005; Sisson and Grove 1993a; Baker and Eggler, 1987; Appendix 3). In a similar way to olivine and clinopyroxene we have also computed the dependence of the An content of crystallizing plagioclase and obtained the following equation

$$\text{Eq.3: } \text{An}(\text{mol}\%) = 0.297T + 5.712H_2O_{\text{melt}} - 3.059\Delta\text{NNO} - 255.968$$

In addition we have also observed that apart of T and H_2O_{melt} , the An content is also dependent on the total crystal content run and according to our results it can be calculated by the following expression:

$$\text{An}(\text{mol}\%) = -0.0756 \cdot T - 0.0324 \cdot H_2O_{\text{melt}} - 0.4645 \cdot \text{crystal content}(\text{wt}\%) + 176.5925$$

Amphiboles

According to the classification of Leake et al. (1997) synthesized amphiboles are ferro-tschermakite to pargasitic hornblendes. The Mg# of experimental amphiboles (calculated with FeOtot) show limited variability with changes in H_2O_{melt} , fO_2 or pressure (Table 8, Fig.14). In contrast to previous findings (i.e., Martel et al. 1999, Scaillet and Evans, 1999; Prouteau and Scaillet, 2003; Pichavant et al. 2002) amphibole crystallizing at 400 MPa has lower Al(IV) content than that at 200 MPa which possibly reflects competition with other high-Al bearing phases, in particular plagioclase (ie., charges 32 and 54).

Fe-Ti oxides

The different Fe-Ti oxide phases present within the charges were recognised by SEM-EDS but, owing to their small size, microprobe analyses were normally contaminated by the surrounding glass, as indicated by the presence of variable K_2O and SiO_2 contents. Fe-Ti oxide modal abundances are low (between 0.1 to 1.5 wt%) in runs conducted at $fO_2 \sim \text{NNO-FMQ}$. Only in runs conducted at high fO_2 (NNO+3.5) do the Fe-Ti oxides abundances exceed 3 wt% (up to 5.5 wt%, Table 3).

Experimental melts

Depending on experimental conditions residual glasses range in compositions from basalt to andesite with only one charge (s0968-18; 1040/200/NNO+3.5, 5 wt% H_2O_{melt}) falling in the trachy-andesite field (Le Bas and Streckeisen 1991). The general trend is to increase the SiO_2 , K_2O , FeO , and TiO_2 contents and decrease Al_2O_3 , CaO and MgO contents, with decreasing H_2O_{melt} (or increasing crystal content) (Fig. 15), a reflection of the crystallising phase assemblage typical of arc magmas (e.g., Sisson and Grove, 1993). At a given H_2O_{melt} a decrease in temperature produces a decrease in FeO^* , CaO and MgO contents and an increase in SiO_2 , TiO_2 , Na_2O and K_2O contents. FeO^* remains almost constant for $H_2O_{\text{melt}} > 6$ wt%, slightly increasing at lower H_2O_{melt} . Experiments at NNO+3.5 produced liquids with the lowest FeO content, owing to profuse oxide crystallisation. In contrast the reduction of fO_2 from NNO to FMQ does not produce significant changes in melt composition, which reflects the facts that a) in almost all NNO and FMQ charges the mineral assemblage is dominated by olivine, clinopyroxene, plagioclase and \pm magnetite (Table 3) and b) the fO_2 values of the NNO and FMQ series overlap to some extent (Table 3). The increase observed in FeO^* and TiO_2 concentrations in runs conducted between $fO_2 \sim$ NNO and FMQ reflects the overall low amounts of crystallizing magnetite (<1.0 wt%) and the lack, or low abundance, of ilmenite. Only when the proportions of these phases exceed 1.5 wt% do the residual melts become FeO depleted. The increase in pressure from 200 to 400 MPa does not produce significant changes in glass composition. However, decreasing pressure from 200 to 100 MPa at constant temperature produces residual melts enriched in SiO_2 , CaO , Al_2O_3 and depleted in FeO^* , in particular at $H_2O_{\text{melt}} < 4$ wt% (Fig. 15).

DISCUSSION

fO_2 conditions needed for tholeiitic vs calc-alkaline trends

Experimental liquids produced by the crystallization of the Santorini basalt define different differentiation trends depending on the prevailing oxygen fugacity. Residual melts obtained at NNO and FMQ show a FeO^*/MgO ratio enrichment with increasing SiO_2 , whereas liquids from experiments conducted at $fO_2 \sim$ NNO+3.5 display much lower FeO^*/MgO which in addition do not vary with melt evolution (see Pichavant et al., 2002). As outlined before, this is due to a combination of different parameters: differences in the crystallizing mineral assemblage, changes in the relative proportions of plagioclase and Fe-Mg bearing minerals, and the composition of these phases. At NNO-FMQ, the ratio plagioclase/Fe-Mg minerals increases with decreasing water content whereas the modal proportion of oxides remains low (Table 3). This drives the liquids toward higher silica and iron contents, coupled to a moderate increase in alkalis, altogether defining a tholeiitic differentiation trend (Miyashiro 1974; Sisson and Grove 1993a, Berndt et al. 2005). In contrast, at high fO_2 ($>NNO+1$) the crystallization of magnetite (>3 wt%) and Fe-Mg minerals in proportions similar to that of plagioclase, in particular at high H_2O_{melt} and temperatures (Table 3), result in an early iron depletion and silica enrichment of the melt (Fig. 15), yielding a typical calc-alkaline liquid

line of descent (Miyashiro 1974; Sisson and Grove 1993a, Pichavant et al., 1999; Berndt et al. 2005).

Magmatic conditions recorded by basalt phenocrysts

A first approximation on the pre-eruptive conditions of Balos Basalt can be retrieved by the comparison between the mineral assemblage of the natural basalt and those from the experimental runs. At $fO_2 \sim NNO$ and $P = 200$ MPa, the co-existence of olivine and orthopyroxene in the same run constraints temperatures to be 990°C and H_2O_{melt} to be 2-3 wt% but, ilmenite is absent at these conditions. When pressure is increased to 400 MPa at such temperature, fO_2 and water contents ilmenite does crystallize but orthopyroxene is lacking (Fig.8 , Table 3). Despite we have not explored $T < 1000^\circ\text{C}$ at such a pressure, previous experimental works conducted in basaltic andesites predict the co-existence of ilmenite and orthopyroxene at $\leq 990^\circ\text{C}$ for $H_2O_{\text{melt}} < 3\text{wt}\%$ although, occurring at expenses of olivine destabilisation (Pichavant et al. 2002). At more reduced conditions ($fO_2 \sim QFM$), pressures of 200 MPa can be ruled out as being those of pre-eruptive as orthopyroxene does not crystallize at the explored range of temperatures and water contents (Fig. 8). In contrast, pressures > 300 MPa and melt water contents $< 4\text{wt}\%$ reproduce the mineral assemblage of the Balos basalt in the explored range of temperatures ($1040\text{--}1000^\circ\text{C}$) although, at such conditions pigeonite is present and the compositions of the natural phases are not matched (Figs. 8c-d; see below). Thus, in a first stage we can conclude that the Balos basalt contained 2-4 wt% H_2O_{melt} but, depending on prevailing fO_2 the range of pre-eruptive T and P are quite variable. To refine such conditions we compare the composition of the natural and experimental phases.

Within the water range constrained before we have found that those experiments conducted at $fO_2 \sim NNO$, $1040\text{--}1000^\circ\text{C}$, 3.5-4wt% H_2O , 100-200MPa closely reproduce the composition of natural olivines (Fo75), plagioclase (An79), diopside ($En_{43}Fs_{11}Wo_{45}$, Mg#80) and crystal content of the natural basalt (40wt%; Figs. 9, 13); whereas natural orthopyroxene is reproduced at somewhat lower temperature (975° , 200 MPa, 3wt% H_2O ; Fig. 12). These two different T values could reflect the cooling down episode followed by the magma and recorded by the natural minerals; notwithstanding, at this oxidation state ($fO_2 \sim NNO$) ilmenite is always absent (Fig.8). In contrast, experiments conducted at FMQ, 1040°C , 400 MPa, 4wt% H_2O closely reproduce the natural mineral assemblage and phase composition when analytical errors are considered however, the crystal content would be higher (75 wt%; Table 3; Fig. 9) than such of the natural basalt (40wt%).

Based on this line of evidences, the probably pre-eruptive conditions for the natural basalt are between $1040\text{--}975^\circ\text{C}$, 100-200MPa, $fO_2 \sim NNO$ and 3-4 wt% H_2O_{melt} ; however, these somewhat wetter conditions inferred for the Balos magma contrast with those constrained for basaltic andesite liquid generation which occur at higher degree of crystallization ($> 60\text{wt}\%$) and lower H_2O_{melt} (2-3 wt%, see below). Thus, if we consider that fractional crystallization is the main mechanism controlling basalt to andesite evolution at Santorini, the H_2O content dissolved in the parental basaltic magmas must be lower than such determined for the more

evolved composition but if this is the case, the prevailing temperature has to be $>1040^{\circ}\text{C}$ to reproduce the natural basalt characteristics (Fig.8).

Although, we have not performed experiments at such conditions, we combined previous temperature estimations in basalts from Santorini ($1085\text{--}1105^{\circ}\text{C}$ Michaud et al. 2000), compositional mineral variations according to changes in experimental variables and equations 1 to 3 obtained in the current work for estimating/calculate the composition of the mineral phases crystallizing at such temperatures. Our calculations show that $T=1100\text{--}1080^{\circ}\text{C}$, $1\text{--}2\text{ wt\% H}_2\text{O}_{\text{melt}}$; $f\text{O}_2\sim\text{FMQ}$ are good estimates of the pre-eruptive conditions as the natural crystal content and phase compositions (olivine, plagioclase, diopside, orthopyroxene) are closely reproduced at such conditions (Figs. 9 to 13). In addition, the T-dependence of orthopyroxene crystallization at 200 MPa and the no coexistence with olivine predicted at 200–400 MPa by similar experimental works (eg, Pichavant et al 2002) points towards a prevailing $f\text{O}_2$ close to FMQ solid buffer and pressures between 300–400 MPa, as the most suitable conditions for reproducing natural basalt characteristics (Fig. 8). However, further experimental work must be performed to refine this estimation.

Origin of Ca-rich plagioclase

Another point of discussion is the presence of Ca-rich plagioclase crystals dispersed within the natural basalt and USC1 andesite having cores of An_{91–89} and narrow rims that frequently match the composition of the main basaltic-andesitic plagioclase population; suggesting re-equilibration with the hosting melt (Figs.2,4). Such plagioclase does not only appear associated to the more mafic compositions, as previous works identified such type of crystals appearing within the more evolved silicic products (dacites, rhyodacites) and mafic enclaves of Santorini (ie, Nichols, 1971; Huijsmann et al. 1988; Michaud et al. 2000; Martin et al. 2006; Gertisser et al. 2009). According to some of these authors such Ca-rich plagioclase may represent the crystallizing products from more mafic magmas at Santorini but however, the conditions of crystallization are not well constrained. Considering the basalt pre-eruptive H_2O content ($1\text{--}2\text{ wt\%}$), a $f\text{O}_2\sim\text{FMQ}$ and using Eq.3, the calculated temperatures for crystallising a plagioclase with An_{91–89} are $1115\text{--}1135^{\circ}\text{C}$, whereas if lower temperatures are considered (i.e., 1080°C) water content must be increased to 4 wt\% to achieve such composition. In fact, calculated conditions for High-Ca plagioclase crystallization are in a good agreement with trapping magma temperatures obtained in inclusions from An₉₀ plagioclases and olivines Fo_{80–76} from basaltic and gabbroic Santorini xenoliths ($1095\pm 20^{\circ}\text{C}$; Michaud et al. 2000.). based on these lines of evidences, we can conclude that An-rich crystals grew from relatively hotter and primitive magmas coming from the mantle which subsequently mixed (totally or partially) with the basaltic to rhyoditic liquids. However the presence of Ca-poor narrow rims matching the Balos composition (and such of the natural andesite; Fig. 7) in the An rich crystals suggests that the crystallization and mixing processes occurred at conditions that differ from those of origin (Figs. 2, 7). According to Nichols, (1971) and Gertisser et al. (2009) mantle derived magmas experience a first stage of crystallization/stagnation at $\geq 800\text{ MPa}$, conditions that probably reflect the An₉₀ crystallization. Later, such Ca-rich plagioclase bearing melts rise to shallower levels (≤ 400

MPa) and mix-mingle with pre-existing basaltic to more evolved melts according to our petrological and experimental results.

Parameters controlling the differentiation trend of basaltic magmas at early stages at Santorini

The comparison between the residual melts from the this work and the information available from the literature concerning the bulk compositions of basaltic to mafic andesitic volcanic rocks is now used to shed light on the parameters controlling the mechanisms of differentiation at Santorini in its early stages.

As previously pointed out, andesitic magmas at Santorini are found either as a major component in the so called intermediate eruptive cycles or as minor component of the so-called silicic eruptions (Nichols, 1971a; Druitt et al., 1999). According to these authors the andesitic melts of these two cycles have different petrological and geochemical affinities. In both cases, erupted rocks are characterised by medium to high K_2O contents but andesites from intermediate cycles have higher FeO^*/MgO ratios and TiO_2 content when compared to those erupted during silicic cycles, falling in the tholeiitic or calc-alkaline fields, respectively (Fig. 16). The general trend of Santorini volcanic rocks is to increase Al_2O_3 , Na_2O and K_2O and decrease MgO and CaO with increasing SiO_2 (Druitt et al. 1999), as in our experiments. In detail, FeO^* , and Al_2O_3 contents increase with differentiation until rock compositions reach ca 55 wt% SiO_2 (basaltic andesite), after which both oxides fall (andesites; Fig 16), which reflect the income of plagioclase and oxides in the crystallisation sequence. Overall, the Santorini rock series are well reproduced by our experimental melts, which suggests that the latter cover P-T- fO_2 - H_2O conditions similar to those in the natural context.

Andesitic liquids (ca 58 wt% SiO_2) have been generated from basalt crystallisation in experiments at 200-400 MPa, 975-1040°C, 4-6.5 wt% H_2O_{melt} , FMQ (Tables 3 and 9), and crystal contents between 60 to 80 wt%. However, the relatively modest change of melt composition with experimental parameters (T, P, H_2O_{melt} , fO_2) makes it difficult to infer the conditions of subsequent melt evolution (ie after andesite composition). The variation of K_2O and FeO^*/MgO with increasing SiO_2 provides some guidance in this respect. At NNO-FMQ and for SiO_2 contents between 52 to 58 wt%, experiments with H_2O_{melt} between 9 to 7wt% (or X_{H_2O} between 1 to 0.7) generally straddle the divide line between calc-alkaline and tholeiitic fields and Low-K / Medium-K series. Only when H_2O_{melt} is between 6 to 2wt% (or X_{H_2O} is between <0.7 and 0.1) do the melts follow the tholeiitic and medium-K features typical of Santorini intermediate andesitic rocks (Table 9; Fig. 16). It is worth noting that in the K_2O vs SiO_2 diagram, melts in charges annealed at 400 MPa, 1000-1040°C, and with H_2O_{melt} between 3-6 wt% clearly fall on the liquid line of descent defined by Santorini rocks (Fig. 16). This contrasts with melts from experiments conducted at higher fO_2 , which run parallel to the trend defined by magmas erupted during silicic cycles, plotting at somewhat lower values.

The above lines of evidence suggest that basaltic andesite to andesitic liquids at Santorini can be generated by 60 to 80 wt% crystallization of a high-alumina parental basalt at temperatures 975-1040°C and 3-6.5 wt% H_2O_{melt} . Changes in fO_2 play an important role on fractionation by

controlling the tholeiitic to calc-alkaline affinity of the magmas. The difference in andesitic magmas between the two different volcanic cycles of Santorini could be the result of a basaltic magma differentiation occurring at different fO_2 , as already suggested by Drüitt et al. (1999). Lastly, the comparison between natural and experimental liquids shows that andesitic melts can be generated over a range of pressures which precludes at this stage any conclusive statement concerning the depth of this stage of evolution. Nevertheless, as shown above, the crystallizing mineral assemblage and the composition of the phases are more sensible to changes in T , P , H_2O_{melt} . In order to refine these constraints, below we compare our experimental results with the phase assemblage and mineral composition from natural basaltic-andesites and andesites.

Conditions for the Upper Scoriae 1 andesitic liquid generation

The petrographic study of the Upper Scoriae 1 andesitic sample allowed us to distinguish different mineral populations within the rock. The main phenocryst assemblage is made of plagioclase (An₅₃), augite (En₄₂Fs₂₁Wo₃₇ Mg# 67), orthopyroxene (En₆₅Fs₂₉ Wo₄, Mg#68) and magnetite which we consider to have crystallized from the andesitic melt. Xenocrysts from a more mafic magma have been identified and include: partially resorbed olivine (Fo₆₈₋₆₄), pigeonite (En₅₅Fs₂₈Wo₁₆ Mg#66 to En₆₀Fs₃₀Wo₈ Mg#66), high-Ca plagioclase (An₉₁₋₈₉), diopside (En₄₃₋₄₅Fs₁₀₋₁₄ Wo₄₃₋₄₅, Mg#75-81) but also, mantled low-Mg orthopyroxene (En₅₅ Fs₄₀ Wo₄, Mg#58), the latter probably coming from a more evolved composition (see above) (Table 2; Figs. 4 to 7).

To a first order approximation, the partially resorbed minerals and mafic cores can be interpreted as testimonies of the conditions of generation of the Upper Scoriae 1 andesitic liquid. Thus, a first constraint on melt generation conditions of USC1 can be made by comparing the xenocrystic mineral assemblage of the natural andesite with the basalt phase equilibrium determined here. The assemblage olivine, augite, plagioclase, orthopyroxene and pigeonite has been only reproduced at 400 MPa, FMQ, $H_2O_{\text{melt}} < 4$ wt% and in the temperature interval 1040-1000°C. Note, however, that at such conditions trace amounts (<0.1 wt%) of ilmenite are present, which is not found in the natural andesite (Fig.8).

The composition of the phases can be used to check and refine this estimate. Experimental olivine from runs conducted at such conditions reproduce the composition of natural xenocrystic olivines (Fo₆₈₋₆₄; Fig. 10). The the xenocrystic pigeonites and orthopyroxene are better reproduced in charges at 1000°C and H_2O_{melt} of 2 rather than at 1040°C which have somewhat higher Mg# (>70; Fig.12). The En contents of experimental orthopyroxene and pigeonite (En₆₄ and En₅₂, respectively), also closely match that of the xenocrysts in andesite (En₆₀ and En₅₅). Water contents of 4 wt% at temperatures between 1040 and 1000°C can be ruled out as the crystallizing orthopyroxene would be too rich in Mg and depleted in Ca when compared with xenocrysts in andesite (Fig. 12). Thus, the olivine, orthopyroxene and pigeonite compositions, all converge to a temperature for basaltic-andesite/andesite generation in the range of 1040-1000°C with H_2O_{melt} around the 2 wt%. At such conditions the plagioclase that crystallizes either at 1040 and 1000°C is An₅₈, being similar to that of the natural andesite. Such a composition occurs as narrow rims on high-Ca xenocryst of

plagioclase and as inner cores on phenocrysts from the USC-1 sample (Fig.7). As for plagioclase, the composition of crystallizing clinopyroxene in charges annealed at 1000°C, 400 MPa and 2 wt% H₂O_{melt} matches that of the natural rock population having En₄₄Fs₁₉Wo₃₇, Mg#70; whereas those from runs at 1040°C are slightly enriched in Mg and somewhat iron depleted, being unlike those found in the natural andesite (En₄₈Fs₁₆Wo₃₅, Mg#75; Table 2; Fig. 11). The fact that the experiments at 400 MPa closely reproduce the xenocrystic assemblage and compositions of the USC1 sample suggests therefore that the USC-1 liquid was generated at such a depth, between 1040-1000°C and at around FMQ. Unfortunately, we could not obtain the residual liquid composition of charges matching the xenocrysts composition but the following suggests that such liquid matches the composition of the USC-1 andesite. The natural andesite composition has been reproduced by 60 to 80 wt% crystallization of the basaltic sample at 200-400 MPa, 975°C, FMQ and 6 wt% H₂O_{melt}, as well as in at 400 MPa, 1040°C, 4 wt% H₂O_{melt} (Fig. 15). However, runs conducted at 200 MPa can be ruled out as being those of natural USC-1 melt generation as the mineral assemblage does not match that of the natural andesite (presence of amphibole, lack of orthopyroxene and pigeonite). At 975°C and 400 MPa the USC1 bulk composition is reproduced at 6 wt% H₂O_{melt} but, under such conditions, amphibole is also present and the liquids have somewhat higher Al₂O₃ content. We have not conducted experiments at lower H₂O contents, as high crystal content and small crystal sizes would make very difficult run product characterisation. Nevertheless, at 975°C and lower H₂O_{melt}, crystallizing phases will have composition clearly different from those of the natural andesite. In particular, olivines (if present) and pyroxenes will have lesser Mg and higher Fe contents thus compositions unlike those of the natural rock.

Thus, we conclude that liquids produced in charges at 1000°C, 400 MPa, 2 wt% H₂O_{melt} and FMQ-0.5 will have somewhat lower Si, Al, Mg; higher Ti, Na, K and similar Fe* and Ca content than experiments conducted at 1040°C, matching altogether the USC-1 bulk composition (Figs. 15 and 16).

Mineralogical evidence for shallow magma reservoir?

The next question is whether these conditions of andesite generation correspond to those prevailing in the reservoir before the eruption, where the main phenocryst phases of andesite have crystallized. The natural andesite contains a mineral assemblage consisting of clinopyroxene, orthopyroxene, plagioclase and magnetite which have been only reproduced at $fO_2 \sim NNO$, 200 MPa, 975°C and H₂O_{melt} < 3 wt% (Fig. 8). At such conditions we could only obtain correct analyses of orthopyroxene due to the high crystal content and small size of phases. The comparison with the natural andesitic orthopyroxene reveals that it has lower Mg#, En and Wo and higher Fs contents than the one crystallized at 200 MPa, 975°C, 3 wt% H₂O_{melt}, $fO_2 \sim NNO$. Moreover, experimental clinopyroxenes synthesized at such a temperature and pressure but at higher bulk water contents (5 wt% H₂O_{melt}) are enriched in Mg and Ca when compared to those from the andesite (Fig. 11, Tables 2 and 5). Otherwise, natural plagioclase is depleted in Ca, compared to those from experiments at such conditions (Table 2

and 7). Although we lack analysis of these phases at low H_2O_{melt} , the results from this work allow us to predict them. The decrease from 3 to ≤ 2 wt% H_2O_{melt} , will decrease the Ca content of plagioclase as well as the Mg content in both clino- and orthopyroxene, producing compositions that would be close to that of the natural andesite (Figs 11 to 13). Although we have not performed experiments at 975°C and 400 MPa and $fO_2 \sim \text{NNO}$, previous experimental works carried out on basaltic andesites under these conditions show that the mineral assemblage clinopyroxene, orthopyroxene, plagioclase and magnetite is stable for H_2O_{melt} between 3.5 and 5 wt% (Pichavant et al. 2002). Thus, we cannot discriminate between 200 and 400 MPa as being that of pre-eruptive conditions and hence, further experimental work has to be performed to constrain the storage conditions of the natural andesite (Andújar et al. in prep). Notwithstanding, these results suggest that a change in the prevailing oxygen fugacity or decrease in pressure+oxidation state may have occurred prior to the eruption of the natural andesite, which would explain the lack of ilmenite observed in the USC-1 sample, since such a phase is not stable at oxydizing conditions ($fO_2 \sim \text{NNO}$) nor at shallower levels (200MPa; Fig.8 this work; Pichavant et al., 2002).

Generation conditions for Santorini basaltic-andesites and andesites

Basaltic andesites from Santorini (54 to 58 wt% SiO_2) share several petrological characteristics regardless they occur as the main erupted component (intermediate cycles) or as a quenched scoriae blebs disseminated within the more silicic compositions (silicic cycles and recent Kameni products). These magmas are characterized by olivine, plagioclase, clinopyroxene, orthopyroxene, Ti-magnetite (\pm ilmenite) phenocrysts (Nicholls, 1971a; Huijsmann et al., 1988; Druitt et al. 1999; Michaud et al. 2000; Martin et al. 2006; Gertisser et al. 2009), set in a groundmass containing clinopyroxene, pigeonite, plagioclase although slight differences in composition and phase proportions occur (Nicholls, 1971a; Huijsmans et al. 1988). Olivine in such basalts is Fo_{70-80} with some minor Fo_{60-65} (Nicholls, 1971a; this work). Plagioclase varies between An_{90} to An_{55-60} whereas orthopyroxene and pigeonite show more restricted compositional variation ($\text{En}_{62-68}\text{Fs}_{29-33}\text{Wo}_{3-4}$) and ($\text{En}_{55-57}\text{Fs}_{25-30}\text{Wo}_{10-15}$) respectively. Clinopyroxenes in such rocks is $\text{En}_{39-44}\text{Fs}_{20-26}\text{Wo}_{36-46}$. Andesitic rocks ($\text{SiO}_2 > 58$ wt%) lack olivine as phenocryst, but this phase occurs as xenocryst along with cores of pigeonite, orthopyroxene and high Ca plagioclase with compositions similar to those found in the more primitives magmas (Nichols, 1971a; Druitt et al. 1999; Martin et al., 2006; this work). *the fact that all these magmas share a similar mineral assemblage can be used to provide accurate constraints on the generation conditions of such magmas beneath the volcano. As we have already pointed out above, our experimental results show that basaltic andesite to andesitic magmas at Santorini can be generated in a wide range of temperatures, pressures, water contents and fO_2 but however, the mineral assemblage (ol+cpx+plag+Ti-mag+opx \pm ilm-pig) and compositions of Santorini basaltic andesites have been experimentally reproduced in this work in a restricted range of conditions: 1000-1040°C; 400MPa, FMQ; in which the residual melt in equilibrium with have SiO_2 contents > 57 wt% and $H_2O_{\text{melt}} \leq 3$ wt%. Actually, these conditions encompass such determined above for USC-1 andesitic liquid generation, which suggests common generation conditions/origin for such magma*

compositions at Santorini. In detail, *the differentiation of high-Al basalts towards a basaltic andesitic magma containing 2-3 wt% H_2O_{melt} occurs at crustal levels (12-15 km depth) by the 60-80wt% crystallization of the mineral assemblage ol+cpx+plag+Ti-mag+opx±pigeonite-ilmenite, at reduced conditions (FMQ-1)*. However, as suggested by the petrology and geochemistry of erupted products, crystal fractionation is not the unique process controlling the compositional evolution at Santorini and crustal assimilation and magma mixing are also involved in the magmatic evolution of such basalts at crustal levels (Huijmans et al. 1988; Druitt et al. 1999). Our temperature, water contents and depths for mafic andesitic magmas generation match previous estimates (Huijmans et al. 1988; Druit et al. 1999; Michaud et al. 2000). However, whether these conditions corresponds to those of rhyodacitic liquids generations (e.g., Gertisser et al. 2009) or if the andesitic to rhyodacitic liquids are stored/generated at shallower levels (e.g., Cottrell et al. 1999; Druitt et al. 1999) cannot be discriminated by our results, and *will be treated in an incoming paper (Andújar et al. in prep)*.

Comparison with ancient series of Akrotiri

The geochemistry of the erupted products the old series of Akrotiri have calc-alkaline affinities compared to the modern series of Thira, which are more tholeiitic (Druitt et al., 1999; Nichols 1971a). Differences between the old and recent series are also found in the petrology as Akrotiri rocks are characterised by the presence of hornblende, suggesting that these magmas evolved under more oxydizing and hydrous conditions, as compared to the younger series (Druitt et al. 1999). Following our results, to produce liquids with a calc-alkaline affinity requires indeed basalt fractionation oxydizing conditions, ($>NNO$ and $<NNO+3.5$). In the explored range of pressures, temperatures and fO_2 , amphibole is stable at $\leq 975^\circ C$ and at $H_2O_{melt} > 3.5$ wt% at $fO_2 \sim NNO$, whereas at more reducing conditions amphibole appears at $H_2O_{melt} > 5$ wt%. Such conditions clearly differ from those inferred above for the youngest series which evolved under somewhat hotter and drier conditions, possibly owing to a change in the source of the magma from the old series to the recent times (ie.; Mortazavi and Sparks 2004).

CONCLUSIONS

The combination between accurate petrological studies and phase equilibria experiments performed on high-Al basaltic sample from Santorini allowed us to constraint the conditions at which basaltic-andesite to andesitic magmas are generated at such volcanic location. Comparison between the andesitic products of Upper Scoriae 1 and those from the literature with our results suggests a range of production conditions for melt basaltic-andesite to andesitic containing 2-3 wt% H_2O between 12-15 km depth, 1040-1000°C, FMQ-1. The evolution from basalts to andesites is controlled by the crystallization of 60-80 wt% of ol+cpx+plag+Ti-mag+opx±pig-ilm but also, by magma mixing and assimilation of host rock processes. However, natural andesites are characterised by the mineral assemblage plagioclase+clinopyroxene+magnetite+orthopyroxene which have been reproduced at higher

oxygen fugacities and at lower pressures indicating that they experience a last episode of equilibration prior to eruption at conditions that are different from those of generation. Moreover, our results agree with those from previous works which suggested that the calc-alkaline or tholeiitic character of santorini magmas is mainly controlled by changes in the prevailing oxydation state. The presence of amphibole in the products from the ancient volcanic edifices (>300 ka) suggests that $fO_2 > NNO$ and water-rich conditions prevailing during their evolution, as suggested by previous works.

REFERENCES

- Andújar, J., Scaillet, B., 2012. Experimental constraints on parameters controlling the difference in the eruptive dynamic of phonolitic magmas: the case from Tenerife (Canary Islands). *Journal of Petrology*. <http://dx.doi.org/10.1093/petrology/EGS033>.
- Baker, D. R. & Eggler, D. H. (1987). Compositions of anhydrous and hydrous melts coexisting with plagioclase, augite, and olivine or low- Ca pyroxene from 1 atm to 8 kbar: application to the Aleutian volcanic center of Atka. *American Mineralogist* 72, 12–28.
- Barclay, J. & Carmichael, I. S. E. (2004). A hornblende basalt from western Mexico: water-saturated phase relations constrain a pressure–temperature window of eruptibility. *Journal of Petrology* 45, 485–506.
- Berndt, J., Koepke, J. & Holtz, F. (2005). An experimental investigation of the influence of water and oxygen fugacity on differentiation of MORB at 200 MPa. *Journal of Petrology* 46, 135–167.
- Burnham, C. W. (1979). The importance of volatiles constituents. In: Yoder, H.S., Jr (ed.). *The evolution of igneous rocks*. Princenton, NJ: Princenton University Press, pp. 439–482.
- Chou, I-M.(1976). Calibration of oxygen buffers at elevated P and T using the hydrogen fugacity sensor. *American Mineralogist* 63, 690–703.
- Cottrell, E., Gardner, J.E. & Rutherford, M.J. (1999). Petrologic and experimental evidence for the movement and heating of the pre-eruptive Minoan rhyodacite (Santorini, Greece). *Contributions to Mineralogy and Petrology* 135, 315–331.
- Deer, W.A.; Howie, R.A. & Zussman, J. (1972). *Rock forming minerals: Framework silicates* 4, 435 pp.
- Di Carlo, I., Pichavant, M., Rotolo, S.G. & Scaillet, B. (2006). Experimental crystallization of a High-K arc basalt: the golden pumice, Stromboli volcano (Italy). *Journal of Petrology* 47, 1317–1343.
- Druitt, T.H., Mellors, R.A., Pyle, D.M., Sparks, R.S.J., 1989. Explosive volcanism on Santorini, Greece. *Geol. Mag.* 126 (2), 95–213.
- Druitt, T.H., Edwards, L., Mellors, R.M., Pyle, D.M., Sparks, R.S.J., Lanphere, M., Davies, M., Barriero, B., 1999. Santorini volcano. *Geological Society of London Memoir*, vol. 19.

165 pp.

Druitt, T. H., Costa, F., Deloule, E., Dungan, M. & Scaillet, B. Decadal to monthly timescales of magma transfer and reservoir growth at a caldera volcano. *Nature* 482, 7780 (2012).

Freise, M., Holtz, F., Nowak, M., Scoates, J.S. & Strauss, H. (2009). Differentiation and crystallization conditions of basalts from the Kerguelen large igneous province: an experimental study. *Contributions to Mineralogy and Petrology* 158, 505-527.

J. E. Gardner & R. M. E. Thomas & C. Jaupart & S. Tait (1996). Fragmentation of magma during Plinian volcanic eruptions. *Bulletin of Volcanology* 58, 144-162.

Gertisser, R., Preece, K. & Keller, J. The Plinian Lower Pumice 2 eruption, Santorini, Greece: Magma evolution and volatile behaviour. *J. Volcanol. Geotherm. Res.* 186, 387-406 (2009).

Huijsmans, J.P.P., 1985. Calc-alkaline lavas from the volcanic complex of Santorini, Aegean Sea, Greece. A petrological, geochemical and stratigraphic study. *Geologica Ultraiectiona* 41, Ph.D. Thesis, 316 pp.

Huijsmans, J.P.P., Barton, M. and Salter, V.J.M., 1988. Geochemistry and evolution of the calc-alkaline volcanic complex of Santorini, Aegean Sea, Greece. *J. Volcanol. Geotherm. Res.*, 34: 283-306.

Kress, V. C. & Carmichael, I. S. E. (1991). The compressibility of silicate liquids containing Fe₂O₃ and the effect of composition, temperature, oxygen fugacity and pressure on their redox states. *Contributions to Mineralogy and Petrology* 108, 82-92.

Leake BE, Woolley AR, Arps CES, Birch WD, Gilbert MC, Grice JD, Hawthorne FC, Kato A, Kisch HJ, Krivovichev VG, Linthout K, Laird J, Mandarino J, Maresch WV, Nickel EH, Schumaker JC, Smith DC, Stephenson NCN, Ungaretti L, Whittaker EJW, Youzhi G (1997) Nomenclature of amphiboles: report of the subcommittee on amphiboles of the International Mineralogical Association Commission on New Minerals and Mineral Names. *Mineral Mag* 61:295-321

Le Bas, M.J., Streckeisen, A.L., 1991. The IUGS systematics of igneous rocks. *Journal of the Geological Society of London* 148, 825-833.

Libourel, G. (1999). Systematics of calcium partitioning between olivine and silicate melt: implications for melt structure and calcium content of magmatic olivines. *Contributions to Mineralogy and Petrology* 136, 63-80.

Martel, C., Pichavant, M., Holtz, F. & Scaillet, B. (1999). Effects of fO₂ and H₂O on andesite phase relations between 2 and 4 kbar. *Journal of Geophysical Research* 104, 29,453-29,470.

Martin, V., Holness, M. & Pyle, D. Textural analysis of magmatic enclaves from the Kameni Islands, Santorini, Greece. *J. Volcanol. Geotherm. Res.* 154, 89-102 (2006).

- Michaud, V., Clocchiatti, R., Sbrana, S., 2000. The Minoan and post-Minoan eruptions, Santorini (Greece), in the light of melt inclusions: chlorine and sulphur behaviour. *Journal of Volcanology and Geothermal Research* 99, 195–214.
- Miyashiro, A., 1974. Volcanic rock series in island arcs and active continental margins. *Am. J. Sci.*, 274:321–355.
- Morgan G. B. & London D. (2005). Effect of current density on the electron microprobe analysis of alkali aluminosilicate glasses. *American Mineralogist* 90, 1131–1138.
- Morimoto N. (1989). Nomenclature of pyroxenes. Subcommittee on pyroxenes. Commission on new minerals and mineral names. *Canadian Mineralogist* 27, 143–156.
- Mortazavi and Sparks (2004). Origin of rhyolite and rhyodacite lavas and associated mafic inclusions of Cape Akrotiri, Santorini: the role of wet basalt in generating calcalkaline silicic magmas. *Contrib Mineral Petrol* 146: 397–413
- Nicholls, I.A., 1971a. Petrology of Santorini volcano, Cyclades, Greece. *J. Petrol.*, 12: 67–119.
- Nichols, I.A. 1971b. Calcareous inclusions in lavas and agglomerates of Santorini volcano. *Contributions to Mineralogy and Petrology* 30, 261–276.
- Papale, P., Moretti, R. & Barbato, D. (2006). The compositional dependence of the saturation surface of H₂O+CO₂ fluids in silicate melts. *Chemical Geology* 229, 78–95
- Parks Michelle M. 1, Juliet Biggs², Philip England¹, Tamsin A. Mather¹, Paraskevi Nomikou³, Kirill Palamartchouk^{1,4}, Xanthos Papanikolaou⁵, Demitris Paradissis⁵, Barry Parsons¹, David M. Pyle^{1*}, Costas Raptakis⁵ and Vangelis Zacharis⁵ (2012). Evolution of Santorini Volcano dominated by episodic and rapid fluxes of melt from depth. *Nature geoscience* 5,749–754.
- Pichavant M., Martel C., Bourdier J.-L. and Scaillet B. (2002). Physical conditions, structure and dynamics of a zoned magma chamber: Mt. Pele'e (Martinique, Lesser Antilles arc). *J. Geophys. Res.* 107(B5), doi:10.1029/ 2001JB000315
- Pichavant, M., Costa, F., Burgisser, A., Scaillet, B., Martel, C & Poussineau, S. (2007). Equilibration scales in silicic to intermediate magmas - Implications for phase equilibrium studies. *Journal of Petrology* 48, 1955–1972
- Pownceby, M.I. & O'Neill, H. St.C. (1994). Thermodynamic data redox reactions at high temperatures.III. Activity-composition relations in Ni-Pd alloys from EMF measurements at 850–1250 K and calibration of the NiO+Ni-Pd assemblage a redox sensor. *Contributions to Mineralogy and Petrology* 116, 327–339.

Robie, R.A., Hemingway, B.S. & Fisher, J.R. (1979). Thermodynamic properties of minerals and related substances at 298.15 K and 1 bar (105 pascals) pressure and at higher temperatures. US Geological Survey Bulletin 1452, 456.

Scailliet, B., Pichavant, M. & Roux, J. (1995). Experimental crystallization of leucogranites magmas. *Journal of Petrology* 36, 663-705.

Sisson, T. W. & Grove, T. L. (1993a). Experimental investigations of the role of H₂O in calc-alkaline differentiation and subduction zone magmatism. *Contributions to Mineralogy and Petrology* 113, 143–166.

Sisson, T. W. & Grove, T. L. (1993b). Temperatures and H₂O contents of low-MgO high-alumina basalts. *Contributions to Mineralogy and Petrology* 113, 167–184.

Toplis, M. J. & Carroll, M. R. (1995). An experimental study of the influence of oxygen fugacity on Fe–Ti oxide stability, phase relations, and mineral–melt equilibria in ferro-basaltic systems. *Journal of Petrology* 36, 1137–1170.

Figure caption

Figure 1. Simplified geological map of Santorini after Druitt et al. (1999) and stratigraphy of the pyroclastic succession of the Thira volcanic showing the silicic or intermediate character of each eruption. We have also indicate the basaltic and andesitic samples selected for performing our work.

Figure 2: a) Scanning electron Microscope (SEM) image of the basaltic starting material. Ol:olivine, Cpx:clinopyroxene, Plag: plagioclase. Mag: magnetic; core to rim compositional profiles of b)olivines, c) natural basalt clinopyroxene and orthopyroxene classification after Morimoto 1989, d) compositional profiles of plagioclases (matrix and xenocrysts) from the Balos basaltic sample.

Figure 3. SEM images of the Upper Scoriae 1 andesitic sample showing a) general view, b) plagioclase xenocrystal c and d) partially reabsorbed olivine xenocrysts, e and f) clinopyroxene xenocrysts.

Figure 4. a) Histogram showing the different populations of clinopyroxene present in the USC-1 andesitic sample as function of their Mg#; b) Histogram showing the En content distribution of main clinopyroxene phenocrysts population (Mg#=67) from the andesitic sample; core to rim compositional profiles of clinopyroxenes from the andesitic sample showing c) Classification of the natural clinopyroxenes and orthopyroxenes of USC-1 ; d) Mg# of clinopyroxene xenocrysts compared to the main andesite phenocrysts composition (Mg#=67; grey line).

Figure 5.a) SEM image of a pigeonite core mantled by a normal-zoned clinopyroxene (crosses are showing EMPA analysis points); b to e) rim to core compositional profiles of pigeonites from the andesitic USC-1 sample. Note the cores mantled by clinopyroxene and the existence of isolated pigeonite crystals within the sample.

Figure 6. SEM images of orthopyroxenes from the USC-1 andesitic sample. a) and b) inversely zoned orthopyroxenes; c) inversely zoned orthopyroxene crystal mantled by a normal-zoning clinopyroxene. (crosses are showing EMPA analysis points).

Figure 7. a) Histogram showing the different populations of plagioclase found within the Upper Scoriae 1 andesitic sample; b) core to rim compositional profiles of USC-1 plagioclase (xenocrysts and matrix crystals).

Figure 8. Phase relations of Balos Basalt from Santorini at a) 200 MPa and $fO_2 \sim NNO$; b) 200 MPa and $fO_2 \sim FMQ$; c) 400 MPa and $fO_2 \sim FMQ$; d) 1000°C and $fO_2 \sim FMQ$ for various temperatures, pressures and water contents in the melt. Ol: olivine, plag: plagioclase, cpx: clinopyroxene, opx: orthopyroxene, pig: pigeonite, amph: amphibole, mag: magnetite, Ti-rich mag: titanium rich-magnetite. Dashed lines are estimated phase boundaries.

Figure 9. Crystal content (wt%) versus H_2O_{melt} (wt%) of experimental runs. Errors are equal to symbol size. Dashed grey line represents the crystal content estimation for the natural Basalt at 1080°C (see text for details).

Figure 10. Composition of experimental olivines (Fo content in moles %) versus a) H_2O (wt%) in co-existing melt; b) Mg# number of co-existing melt; c) CaO (wt%) in olivines versus H_2O_{melt} ; d) Fo content in moles (%) versus CaO/ Al_2O_3 ratio in co-existing melt; e) Fo content in moles (%) versus CaO (wt%) in olivines. Number next to symbols in the legend indicate temperature (°C), pressure (MPa) and prevailing fO_2 conditions. Dashed grey line represents the calculated olivine composition by equation 1 for the natural Basalt at 1080°C (see text for details).

Figure 11. Compositional variation of experimental clinopyroxenes. a) Mg# variation; b) En content variation; c) Fs content variation; d) Wo content variation. Number next to symbols in the legend indicate temperature (°C), pressure (MPa) and prevailing fO_2 conditions. Dashed grey line represents the clinopyroxene composition estimation (plates a to c) and calculated (d) for the natural Basalt at 1080°C (see text for details).

Figure 12. Compositional variation of experimental orthopyroxenes and pigeonites. a) Classification experimental orthopyroxenes and pigeonites; b) Mg# variation; c) En content variation; d) Fs content variation; e) Wo content variation. Number next to symbols in the legend indicate temperature (°C), pressure (MPa) and prevailing fO_2 conditions.

Figure 13. Compositional variation of experimental plagioclase. a) An content (in moles%) versus H_2O_{melt} wt%; b) Or content (in moles%) versus H_2O_{melt} wt%; c) An content (in moles%) versus crystal content (wt%). Number next to symbols in the legend indicate temperature (°C), pressure (MPa) and prevailing fO_2 conditions. Dashed grey line represents the calculated (plate a) and estimated (plate b) plagioclase composition estimation for the natural Basalt at 1080°C (see text for details).

Figure 14. Composition of experimental amphiboles. a) Al (IV) versus cations in A site; b) Al (IV) versus Mg# in amphibole. Structural formulae calculated as in Leake (1997). Number next to symbols in the legend indicate temperature (°C), pressure (MPa) and prevailing fO_2 conditions.

Figure 15. (a-h) Glass compositional variations in major and minor oxides with water content in the melt. Grey horizontal bar shows the natural USC-1 andesite bulk-rock composition.

Figure 16 a) Tholeiitic and calc-alkaline affinities of Santorini magmas (Silicic and intermediate dominated compositions) and experimental melts. b) TiO_2 , c) FeO^* and d) K_2O versus SiO_2 (wt%) of Santorini magmas and experimental melts. Natural rock Data from Druitt et al. (1999).

Appendix 1.

core to rim compositional profile of a) En content in xenocrystic clinopyroxene in Natural Balos basalt; core to rim compositional profiles of clinopyroxenes from the andesitic sample showing b) En content; c) Fs content; d) Wo content and compared to the main phenocrysts composition of USC-1 andesite (Mg#=67; grey line).

Appendix 2

a) Experimental Kd Fe-Mg clinopyroxene-glass versus Mg# of co-existing glass.

b) Ca/Na in experimental plagioclase and co-existing glass. Lines show approximate Kds from Sisson and Grove (1993).

Table 1 : Major element composition of the natural Balos basalt sample: bulk-rock, starting material and mineral phases

	Bulk-rock	Starting material	SD magnetite		SD ilmenite		SD olivine		SD diopside		SD opx		SD plag		SD plag xeno		SD
<i>n</i> :	10		7		5		32		29		2		37		9		
SiO ₂	51.1	51.8	0.2	0.11	0.06	0.03	0.03	37.69	0.45	48.81	1.51	53.29	0.19	47.70	0.47	45.05	0.45
TiO ₂	0.91	0.96	0.04	7.88	0.84	50.47	1.88	0.02	0.03	0.89	0.17	0.44	0.08	0.03	0.02	0.02	0.02
Al ₂ O ₃	18.2	17.7	0.2	2.67	1.11	0.09	0.04	0.01	0.02	5.03	1.54	0.72	0.01	31.75	0.26	33.62	0.22
MgO	6.77	6.53	0.09	0.96	0.71	1.18	0.32	35.73	0.71	14.45	0.93	23.58	0.22	0.05	0.02	0.03	0.02
CaO	11.2	11.2	0.2	0.16	0.16	0.04	0.04	0.19	0.09	20.95	1.79	3.72	0.10	15.95	0.27	17.98	0.23
MnO	0.16	0.09	0.05	0.21	0.15	0.49	0.11	0.48	0.07	0.21	0.15	0.49	0.14	0.02	0.02	0.03	0.04
FeO _{tot}	8.21	8.28	0.22	87.99	2.32	47.69	2.23	21.09	0.65	6.48	0.75	13.66	0.31	0.61	0.08	0.45	0.08
Na ₂ O	2.83	2.74	0.06	0.00	0.00	0.01	0.01	0.01	0.01	0.32	0.06	0.04	0.01	2.29	0.13	1.20	0.07
K ₂ O	0.5	0.57	0.05	0.02	0.02	0.03	0.03	0.01	0.02	0.05	0.23	0.00	0.00	0.12	0.03	0.03	0.01
P ₂ O ₅	0.13	0.20	0.08	—	—	—	—	—	—	—	—	—	—	—	—	—	—
Sum	100.04	100		100.0	0.0	100.0	0.0	95.3	0.8	97.2	1.7	95.9	1.0	98.5	0.5	98.40	0.56
Mg#				1.9	0.5	1.4	0.5	—	—	79.9	1.6	75.5	0.2				
<i>Mol %</i>																	
Fo							74.9	1.1									
En									43.4		2.6	69.0	0.5				
Fs									10.9		1.2	22.4	0.1				
Wo									45.3		3.5	7.8	0.1				
An														78.8	1.2	89.07	0.66
Ab														21.5	1.7	10.78	0.65
Or														0.8	0.2	0.15	0.06
Phase																	
proportions (wt %)				trace		trace	6.6		1.9		trace		31.5				

- Bulk-rock analysed by inductively coupled plasma mass spectrometry. *n*, number of analyses. SD, standard deviation. FeO_{tot}, total iron reported as FeO. Fo (mol %) = 100 Mg/(Mg + Fe_{tot}) in olivine. En, Fs and Wo were calculated as in the study by Morimoto (1989). Mg# = 100[Mg/(Mg + Fe_{tot})]. An = 100[Ca/(Ca + Na + K)]; Ab = 100[Na/(Ca + Na + K)]; Or = 100[K/(Ca + Na + K)]. End-members calculated as in the study by Deer *et al.* (1972). trace, crystal abundance <0.5 wt %. opx, orthopyroxene; plag, plagioclase; xeno, xenocryst.

Table 2 : Major element composition of the natural Upper Scoria 1 andesite sample: bulk-rock, starting material and mineral phases

	Bulk-rock	glass*	magnetite	SD	plag	SD	augite Mg# 67	SD	augite Mg# 70	SD	augite Mg# 63	SD	opx	SD	
<i>n</i> :	6			85			67		17		11		5		
SiO ₂	58.52	62.79	0.11	0.02	55.05	1.44	49.25	0.73	48.97	1.14	48.38	1.41	52.05	0.72	
TiO ₂	1.30	0.98	15.14	2.29	0.07	0.13	1.01	0.12	0.97	0.13	1.10	0.46	0.33	0.06	
Al ₂ O ₃	16.04	15.82	3.02	0.56	26.61	0.74	3.54	0.66	3.02	0.64	3.36	1.41	1.09	0.51	
MgO	2.84	1.78	2.64	0.50	0.08	0.11	14.20	0.44	14.65	0.32	12.70	0.72	23.49	0.77	
CaO	6.55	4.82	0.07	0.06	10.40	0.54	17.46	0.81	17.36	0.72	18.28	1.03	2.09	0.19	
MnO	0.19	0.19	0.50	0.22	0.04	0.05	0.42	0.12	0.37	0.08	0.51	0.16	0.63	0.10	
FeO _{tot}	8.74	7.01	71.45	1.34	0.62	0.57	12.40	0.50	11.09	0.28	13.55	0.86	18.85	0.69	
Na ₂ O	4.19	4.70	0.03	0.04	5.03	0.31	0.31	0.05	0.23	0.03	0.31	0.10	0.07	0.10	
K ₂ O	1.40	1.90	0.02	0.03	0.20	0.11	0.02	0.02	0.02	0.02	0.06	0.13	0.02	0.03	
P ₂ O ₅	0.23														
Sum	100	100	93.09	1.60	98.27	1.37	92.68	1.21	96.81	0.83	98.36	1.02	98.77	1.32	
Mg#			6.2	0.40			67.12	0.62	70.18	0.37	62.56	1.38	68.96	0.84	
<i>mol %</i>															
En							41.83	1.07	43.65	0.94	37.64	1.45	65.38	0.86	
Fs							20.50	0.70	18.54	0.45	22.53	1.15	29.43	0.81	
Wo							36.98	1.65	37.18	1.36	38.97	2.12	4.19	0.41	
An					52.66	2.48									
Ab					46.10	2.50									
Or					1.24	0.75									
	olivine	SD	olivine	plag	SD	opx	SD	pig	SD	pig	SD	diopside	SD	diopside	SD
<i>n</i> :	3		1	25		18		6		8		5		5	
SiO ₂	35.84	0.09	34.02	44.89	1.00	50.60	1.12	52.53	0.90	50.56	1.01	51.26	0.26	50.39	0.37

	Bulk-rock	glass*	magnetite	SD	plag	SD	augite Mg# 67	SD	augite Mg# 70	SD	augite Mg# 63	SD	opx	SD	
<i>n</i> :			6		85		67		17		11		5		
TiO ₂	0.04	0.04	0.00	0.03	0.03	0.28	0.09	0.23	0.07	0.56	0.16	0.46	0.03	0.65	0.10
Al ₂ O ₃	0.01	0.01	0.00	33.36	0.51	0.66	0.15	0.73	0.26	1.98	0.42	2.81	0.34	2.87	0.12
MgO	30.82	0.56	35.62	0.09	0.21	19.01	0.47	20.99	0.91	19.22	0.86	15.04	0.26	13.94	0.31
CaO	0.23	0.09	0.15	17.82	0.54	1.84	0.18	3.92	0.52	7.74	1.15	21.26	0.29	20.34	0.20
MnO	0.75	0.13	0.82	0.03	0.04	1.02	0.19	0.74	0.08	0.69	0.18	0.13	0.13	0.13	0.10
FeO _{tot}	31.58	0.21	29.53	0.55	0.17	24.94	0.48	18.80	0.87	17.42	0.79	6.20	0.31	8.27	0.22
Na ₂ O	0.02	0.04	0.05	1.01	0.30	0.03	0.03	0.06	0.04	0.12	0.05	0.19	0.02	0.26	0.04
K ₂ O	0.02	0.02	0.00	0.02	0.02	0.01	0.01	0.03	0.03	0.03	0.02	0.01	0.01	0.01	0.02
P ₂ O ₅															
Sum	99.5	0.3	100.3	98.1	1.2	98.5	1.6	98.9	0.7	98.4	1.2	97.7	0.4	97.2	0.6
Mg#						57.6	0.7	66.6	0.7	66.3	0.6	81.2	0.8	75.0	0.6
<i>Mol %</i>															
Fo	63.5	0.5	68.3												
En						54.5	0.9	60.4	0.7	55.0	1.9	44.4	0.5	41.9	0.5
Fs						40.1	0.6	30.3	0.8	28.0	0.9	10.3	0.5	13.9	0.3
Wo						3.8	0.4	8.1	0.9	15.9	2.5	45.1	0.7	43.9	0.4
An				90.6	2.7										
Ab				9.3	2.7										
Or				0.1	0.1										

- *Composition of residual glass calculated by mass-balance (see text for details).
- Bulk-rock analysed by inductively coupled plasma mass spectrometry. *n*, number of analyses; SD, standard deviation. FeO_{tot}, total iron reported as FeO. Fo (mol %) = 100[Mg/(Mg + Fe_{tot}) in olivine. En, Fs and Wo were calculated as in the study by Morimoto (1989). Mg# = 100[Mg/(Mg + Fe_{tot})]. An = 100[Ca/(Ca + Na + K)]; Ab = 100[Na/(Ca + Na + K)]; Or = [100K/(Ca + Na + K)]. End-members calculated as in the study by Deer *et al.* (1972). opx, orthopyroxene; pig, pigeonite.

Table 3 : Experimental run conditions and results

Run	XH ₂ O _{in}	H ₂ O*	H ₂ O†	log fO ₂	ΔNNO	ΔQFM	Phase assemblage										
	(moles)	(wt %)	(wt %)	(bar)			Ol	Cpx	Mag	Plag	Opx	Pig	Ilm	Amph	Crystal	Gl	Σr ²
NNO experiments																	
<i>1040°C, 200 MPa, 24.5 h, fH₂ (bar): 9.5 calc</i>																	
				-9.30	0.04												
s0968-1	1.00	6.30	5.95	-9.62	0.10										0.0	100.0	
s0968-2	0.75	5.45	7.43	-9.43	0.28		4.82	10.74	0.83	18.42					34.8	65.2	0.45
s0968-3	0.50	4.47	6.85	-9.42	0.29		4.52	11.81	0.12	24.21					40.7	59.3	0.38
s0968-4	0.34	3.65	5.93	-9.53	0.18		6.22	17.54	0.05	32.51					56.2	43.8	0.48
s0968-5	0.10	1.40	2.83	— 10.31	-0.60		7.99	18.91	0.46	56.05					83.4	16.6	0.69
<i>1000°C, 200 MPa, 27 h, fH₂ (bar): 9.73</i>																	
				— 10.00	0.33												
s0968-6	1.00	6.30	5.94	— 10.33	-0.04		4.09	16.70	2.40	29.66					52.8	47.2	0.25
s0968-7	0.67	5.16		— 10.75	-0.53		X	X	X	X							
s0968-9	0.50	4.44	2.85	— 11.10	-0.81		6.74	21.30	1.24	37.27					66.6	33.4	0.32
s0968-10	0.34	3.67		— 11.65	-1.43		X	X	X	X							
s0968-11	0.10	1.40		—	—		X	X	X	X							
<i>1040°C, 100 MPa, 28 h, fH₂ (bar): 6.11</i>																	
				-9.54	0.20												
s0968-12	1.00	4.30	6.63	-9.74	-0.01		4.46	14.11	0.49	20.33					39.4	60.6	0.22
s0968-13	0.70	3.60	6.30	-9.71	0.02		6.27	15.80	1.42	34.63					58.1	41.9	0.15

Run	XH ₂ O _{in}	H ₂ O ⁺	H ₂ O ⁺	log fO ₂	ΔNNO	ΔQFM	Phase assemblage										
	(moles)	(wt %)	(wt %)	(bar)			Ol	Cpx	Mag	Plag	Opx	Pig	Ilm	Amph	Crystal	Gl	Σr ²
s0968-14	0.49	3.00	3.40	— 10.41	−0.68		7.08	16.90	1.47	35.62					61.1	38.9	0.29
s0968-15	0.29	2.33	2.17	— 11.38	−1.65		X	X	X	X							
s0968-16	0.10	0.96		—	—		X	X	X	X							
1040°C, 200 MPa, 31 h, fH ₂ (bar): 0.2 calc																	
				−5.98	3.73												
s0968-17	1.00	6.30	6.30	−5.98	3.73			12.67	3.29						16.0	84.0	0.23
s0968-18	0.72	5.35	4.55	−6.26	3.45		trace	22.30	4.55	36.60	2.09				65.5	34.5	0.21
s0968-19	0.52	4.52		−6.55	3.17			X	X	X	X						
s0968-20	0.33	3.63		−6.94	2.77			X	X	X	X						
s0968-21	0.10	1.40		−7.82	1.89												
975°C, 200 MPa, 23.5 h, fH ₂ (bar): 4.50																	
				−9.76	0.52												
s0968-22	1.00	6.30		−9.76	0.92				X	X				X			
s0968-23	0.71	5.31		— 10.06	0.62		X	X	X	X				X			
s0968-24	0.52	4.55		— 10.33	0.35		X	X	X	X				X			
s0968-25	0.33	3.62		— 10.72	−0.05			X	X	X	X						
s0968-26	0.10	1.40		— 11.41	−0.73			X	X	X	X						
1000°C, 400 MPa, 30 h, fH ₂ (bar): 16.36																	
				−9.77	0.56												
s0968-27b	1.00	8.98		−9.77	0.49		X	X	X	X							

Run	XH ₂ O _{in}	H ₂ O ⁺	H ₂ O ⁺	log fO ₂	ΔNNO	ΔQFM	Phase assemblage										
	(moles)	(wt %)	(wt %)	(bar)			Ol	Cpx	Mag	Plag	Opx	Pig	Ilm	Amph	Crystal	Gl	Σr ²
s0968-28b	0.74	7.71	6.83	−9.86	0.39		7.64	13.08	0.99	27.10					48.8	51.2	0.09
s0968-29b	0.53	6.52	6.69	−9.94	0.31		9.65	18.67	1.12	30.73					60.2	39.8	0.08
s0968-30b	0.30	4.88		— 10.09	0.13		X	X	X	X			X				
s0968-31b	0.10	2.00		— 10.20	0.02		X	X	X	X			X				

QFM experiments

1000°C, 400 MPa, 28 h, fH₂ (bar): 33.32

				— 10.39	-0.06	0.46											
s0968-37	1.00	8.98		— 10.39	-0.06	0.46	X	X	X								
s0968-38	0.69	7.44		— 10.40	-0.07	0.45	X	X	X	X			X				
s0968-39	0.59	6.92	7.60	— 10.45	-0.12	0.55	6.33	19.82	0.78	28.87			trace		55.7	44.3	0.05
s0968-40	0.29	4.82		— 11.04	-0.71	-0.19	X	X	X	X	X	X	X				
s0968-41	0.10	2.00		— 11.63	-1.30	-0.78	X	X	X	X	X	X	X				

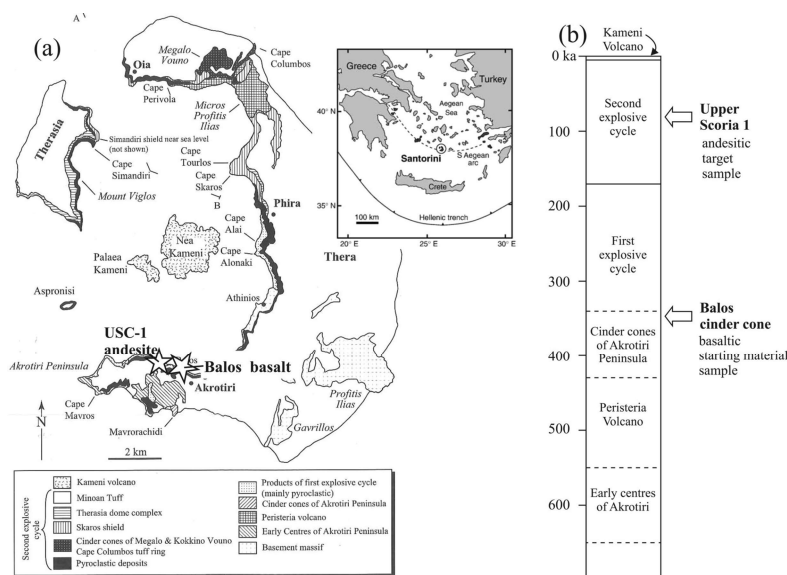
1000°C, 200 MPa, 21 h, fH₂ (bar): 13.69

				— 10.29	0.04	0.55											
s0968-42	1.00	6.30	7.53	— 10.41	-0.08	0.44	5.70	9.33	0.26	16.28					31.6	68.4	0.13
s0968-43	0.94	6.10	7.72	— 10.36	-0.03	0.49	6.89	8.86	0.80	21.34					37.9	62.1	0.03
s0968-44	0.84	5.76	7.06	— 10.44	-0.11	0.41	7.54	12.06	1.45	35.00			0.91		55.1	44.9	0.45

Run	XH ₂ O _{in}	H ₂ O [*]	H ₂ O†	log fO ₂	ΔNNO	ΔQFM	Phase assemblage											
	(moles)	(wt %)	(wt %)	(bar)			Ol	Cpx	Mag	Plag	Opx	Pig	Ilm	Amph	Crystal	Gl	ΣI ²	
s0968-45	0.72	5.35		— 10.80	−0.47	0.05	X	X	X	X			X					
s0968-46	0.54	4.63		— 11.05	−0.72	−0.20	X	X	X	X			X					
975°C, 200 MPa, 24.5 h, fH ₂ (bar): 53.54																		
				— 11.91	−1.58	−0.69												
s0968-32	1.00	6.30	7.10	— 11.97	−1.26	−0.75	4.94	14.63	1.18	24.61				10.74	56.1	43.9	0.07	
s0968-33	0.73	5.36		— 12.26	−1.55	−1.04	X	X	X	X			X					
s0968-34	0.51	4.51		— 12.84	−2.13	−1.62	X	X	X	X			X					
s0968-35	0.28	3.34		— 13.91	−3.20	−2.69	X	X	X	X			X					
s0968-36	0.10	1.40		— 14.50	−3.79	−3.28	X	X	X	X			X					
1040°C, 400 MPa, 23 h, fH ₂ (bar): 26.86																		
				−9.54	0.20	0.73												
s0968-47	1.00	8.98	6.48	−9.86	−0.12	0.41	1.31	8.56	0.49						10.4	89.6	0.67	
s0968-48	0.70	7.54		−9.95	−0.21	0.32	X	X	X	X								
s0968-49	0.58	6.86		−9.97	−0.23	0.30	X	X	X	X	X	X						
s0968-50	0.30	4.92	4.77	−9.98	−0.24	0.29	11.88	20.20	1.29	43.01	trace	trace			76.6	23.4	0.18	
s0968-51	0.10	2.00		— 10.27	−0.53	0.00	X	X	X	X	X	X	X					
975°C, 400 MPa, 35 h, fH ₂ (bar): 87.55																		
				— 11.55	−0.84	−0.33												
s0968-52	1.00	8.89			−0.95	−0.44			X						X			

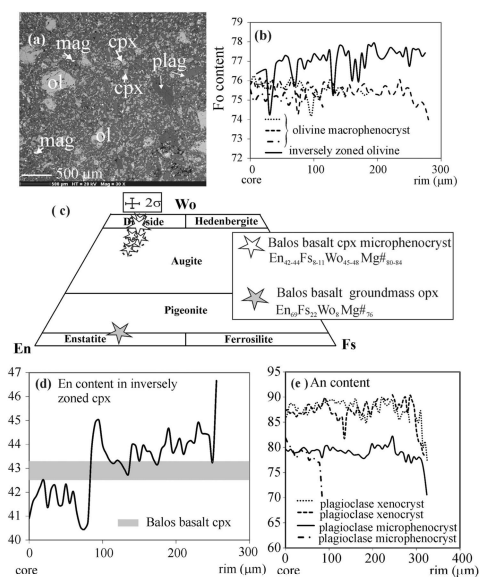
Run	XH ₂ O _{in}	H ₂ O [*]	H ₂ O [†]	log fO ₂	ΔNNO	ΔQFM	Phase assemblage										
	(moles)	(wt %)	(wt %)	(bar)			Ol	Cpx	Mag	Plag	Opx	Pig	Ilm	Amph	Crystal	Gl	Σr ²
				11.66													
s0968-53	0.93	8.55	—	11.72	−1.01	−0.50		X	X	X				X			
s0968-54	0.70	6.89	6.40	—	−1.21	−0.75	10.65	18.88	trace	37.65				0.86	68.0	32.0	0.83
				11.92													

- *Water content in the melt determined by the solubility model of Papale *et al.* (2006) using the method of Scaillet & Macdonald (2006).
- $\dagger H_2O$ determined with the by-difference method (see text for details).
- XH_2O_{in} , initial $H_2O/(H_2O + CO_2)$ in the charge. f_{H_2} (bar), hydrogen fugacity of the experiment, determined using NiPd or CoPd alloy sensors; calc, calculated using the data obtained from successful NiPd or CoPd alloys (see text for details). $\log f_{O_2}$ (bar), logarithm of the oxygen fugacity calculated from the experimental f_{H_2} . $\Delta NNO/\Delta QFM$, $\log f_{O_2} - \log f_{O_2}$ of the NNO or QFM buffer calculated at P and T (NNO: Pownceby & O'Neill, 1994; QFM: Chou, 1978). Crystal content, values indicate the phase abundance in the charge (in wt %). Gl, glass; Ol, olivine; Cpx, clinopyroxene; Mag, magnetite; Plag, plagioclase; Opx, orthopyroxene; Pig, pigeonite; Ilm, ilmenite; Amph, amphibole; trace, phase with a modal abundance <0.1 wt %; X, phase identified using SEM.



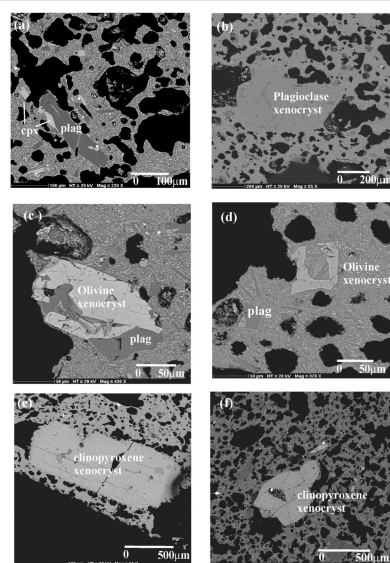
Joan Andújar et al. J. Petrology 2015;56:765-794

Petrography and mineral chemistry of the Balos basalt sample.



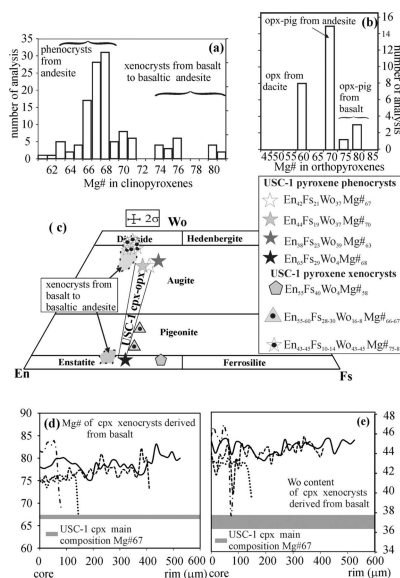
Joan Andújar et al. J. Petrology 2015;56:765-794

Back-scattered electron images of the Upper Scoria 1 andesitic sample, showing (a) general view, (b) plagioclase xenocryst, (c, d) partially resorbed olivine xenocrysts, and (e, f) clinopyroxene xenocrysts.



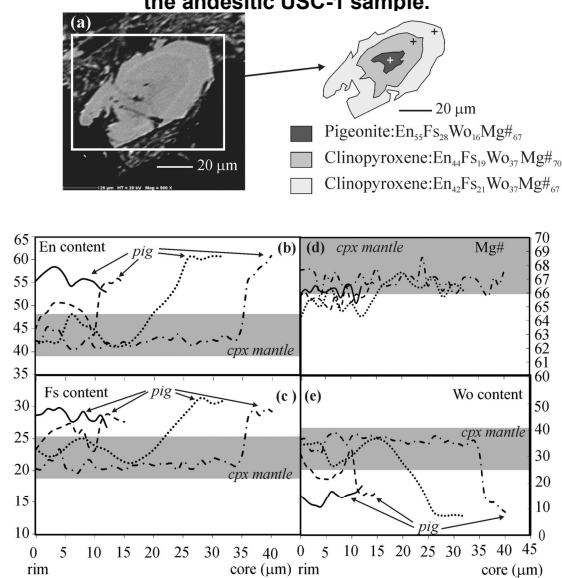
Joan Andújar et al. *J. Petrology* 2015;56:765-794

(a, b) Histograms showing the populations of clinopyroxene and orthopyroxene present in the USC-1 andesite sample as functions of Mg#; the populations are labelled with interpretations discussed in the text; (c) compositions of clinopyroxene and orthopyroxene in USC-1, plotted onto the classification diagram of Morimoto (1989); tie-lines for the main cpx-opx populations are shown; those found in basaltic samples are also shown for comparison; (d) Mg# and (e) Wo content profiles across clinopyroxene xenocrysts in the USC-1 sample compared with the main andesite phenocryst composition (grey bands).



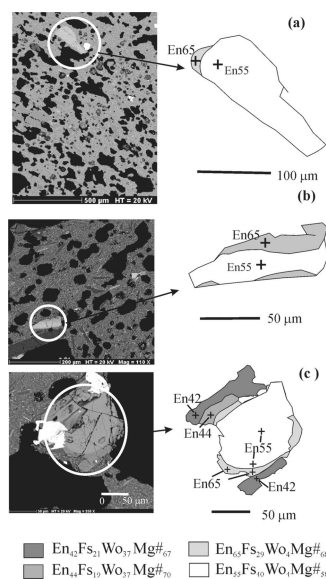
Joan Andújar et al. *J. Petrology* 2015;56:765-794

(a) Back-scattered electron image of a pigeonite core mantled by normally zoned clinopyroxene (crosses show EMP analysis points); (b–e) rim to core compositional profiles of pigeonite from the andesitic USC-1 sample.



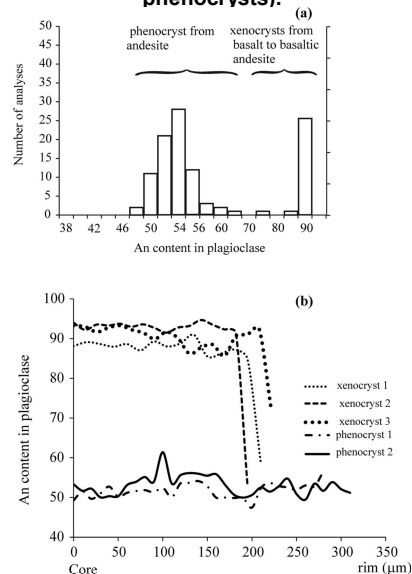
Joan Andújar et al. J. Petrology 2015;56:765-794

Back-scattered electron images of orthopyroxene from the USC-1 andesitic sample.



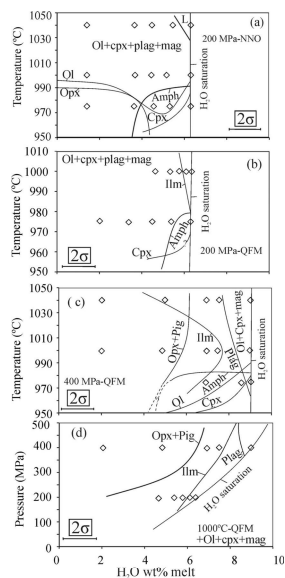
Joan Andújar et al. J. Petrology 2015;56:765-794

(a) Histogram showing the populations of plagioclase found within the Upper Scoria 1 andesitic sample; (b) core to rim compositional profiles of USC-1 plagioclase (xenocrysts and phenocrysts).



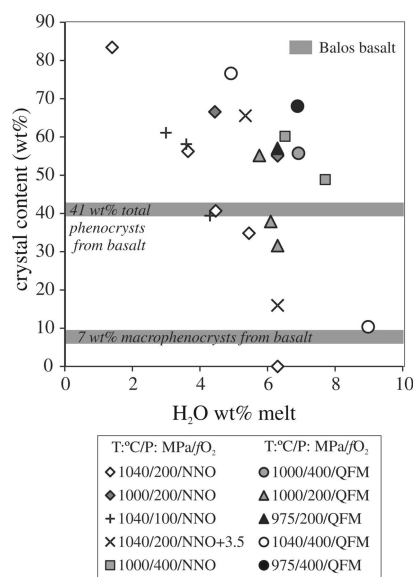
Joan Andújar et al. *J. Petrology* 2015;56:765-794

Phase relationships of the Balos basalt at (a) 200 MPa and $fO_2 \sim NNO$, (b) 200 MPa and $fO_2 \sim QFM$, (c) 400 MPa and $fO_2 \sim QFM$, and (d) 1000°C and $fO_2 \sim QFM$, as a function of temperature, pressure and water content in the melt. ol, olivine; plag, plagioclase; cpx, clinopyroxene; opx, orthopyroxene; pig, pigeonite; amph, amphibole; mag, magnetite.



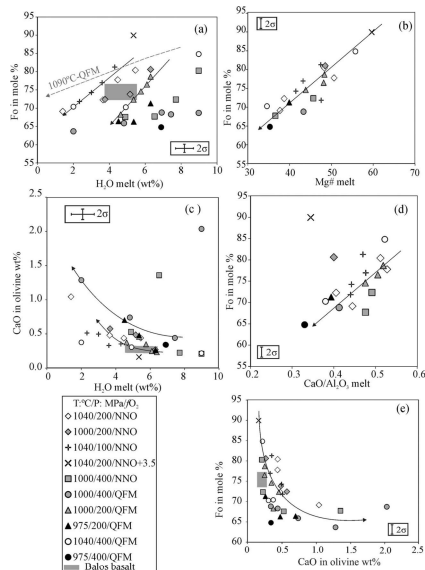
Joan Andújar et al. *J. Petrology* 2015;56:765-794

Crystal content (wt %) vs H₂O melt (wt %) for the experimental runs.



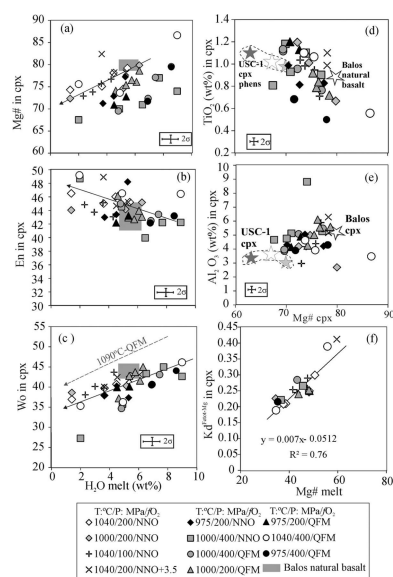
Joan Andújar et al. J. Petrology 2015;56:765-794

Compositions of experimental olivines (Fo content in mol %) vs (a) H₂O (wt %) in the coexisting melt and (b) Mg# number of the coexisting melt; (c) CaO (wt %) in olivine vs H₂O melt.



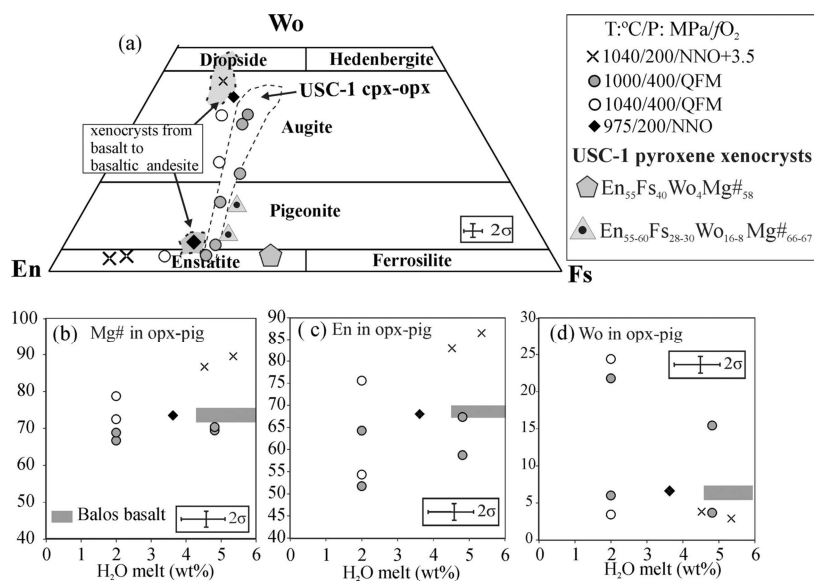
Joan Andújar et al. J. Petrology 2015;56:765-794

Compositional variation of experimental clinopyroxene.



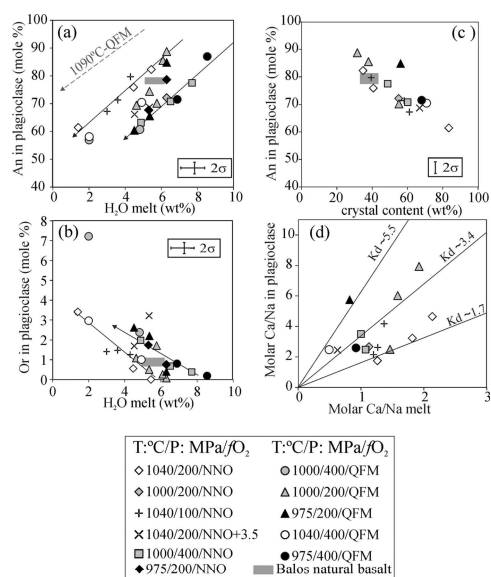
Joan Andújar et al. J. Petrology 2015;56:765-794

Compositional variation of experimental pyroxenes.



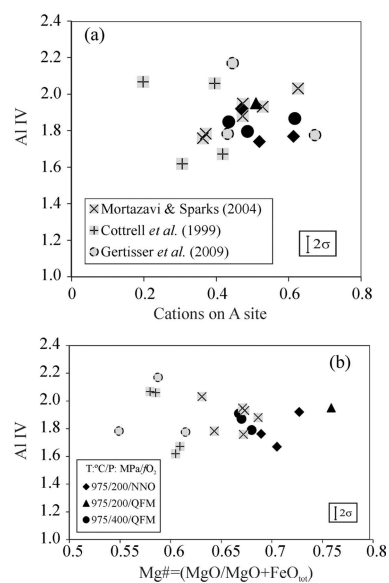
Joan Andújar et al. J. Petrology 2015;56:765-794

Compositional variation of the experimental plagioclase.



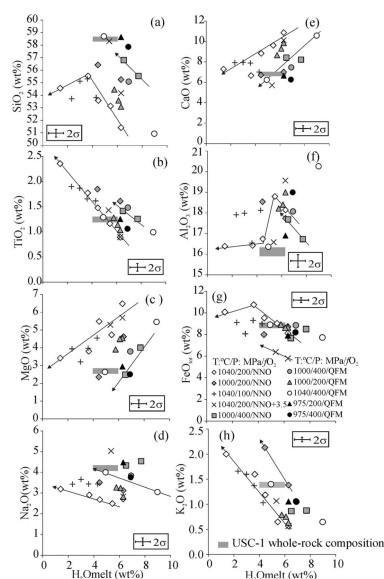
Joan Andújar et al. *J. Petrology* 2015;56:765-794

Compositions of experimental amphibole (black symbols) compared with those from Santorini eruptive products (grey symbols).



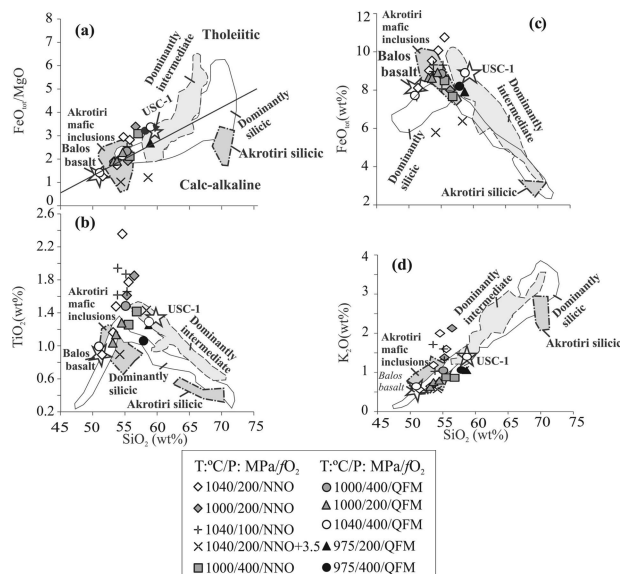
Joan Andújar et al. *J. Petrology* 2015;56:765-794

(a–h) Experimental glass compositional variations of major and minor oxides with water content in the melt.



Joan Andújar et al. J. Petrology 2015;56:765-794

(a) Tholeiitic vs calc-alkaline affinities of Santorini eruptive products (silicic and intermediate compositions) and experimental melts.



Joan Andújar et al. J. Petrology 2015;56:765-794